A TM7 conformational switch governs GPCR transducer selectivity

Guodong He[1,2,3,13]*, Maik Pankonin[4,13], Guojing Yu[1,2,3,13], Haiyan Xu[5,13], Huan Li[3,13], Maximilian Salomon[4], Hossein Batebi[4,6], Xue Guo[7], Shuhao Zhang[1,2,3], Fang Kong[1,2,8], Li Zhan[5], Xiaoou Sun[1,2,9], Qingqing Ma[10], Lan Hua[3], Sheng Ding[3], Chuangye Yan[1,2,8], Xin Chen[7], Zhaobing Gao[5]*, Peter W. Hildebrand[4,11]*, and Xiangyu Liu[1,2,3,12]*

[1]State Key Laboratory of Membrane Biology, Tsinghua-Peking Center for Life Sciences, Tsinghua University, Beijing, China.

[2]Beijing Frontier Research Center for Biological Structure, Beijing Advanced Innovation Center for Structural Biology, Tsinghua University, Beijing, China.

[3]School of Pharmaceutical Sciences, Tsinghua University, Beijing, China.

[4]Institute of Medical Physics and Biophysics, Medical Faculty, Leipzig University, Leipzig, Germany

[5]State Key Laboratory of Drug Research, Shanghai Institute of Materia Medica, Chinese Academy of Sciences, Shanghai 201203, China.

[6]Department of Physics, Freie Universität Berlin, 14195, Berlin.

[7]School of Pharmacy, Changzhou University, Changzhou, China

[8]School of Life Sciences, Tsinghua University, Beijing, China.

[9]School of Basic Medical Sciences, Tsinghua University, Beijing, China.

[10]Protein Chemistry and Proteomics Platform, Tsinghua University

[11]Center for Scalable Data Analytics and Artificial Intelligence (ScaDS.AI), Leipzig, Germany.

[12]Beijing Key Laboratory of Cardiovascular Receptors Research, Peking University, Beijing, China.

[13]These authors contributed equally to this work: Guodong He, Maik Pankonin, Guojing Yu, Haiyan Xu and Huan Li.

*Corresponding authors: Guodong He (hgd@mail.tsinghua.edu.cn), Zhaobing Gao (zbgao@simm.ac.cn), Peter W. Hildebrand (peter.hildebrand@medizin.uni-leipzig.de) and Xiangyu Liu (liu_xy@mail.tsinghua.edu.cn).

Abstract:

Deciphering transducer selectivity in G protein-coupled receptors (GPCRs) is essential for developing next-generation therapeutics with improved safety profiles. Here, we identify *(R)*-**141**, a μ-opioid receptor (μOR) agonist with a distinct scaffold that exhibits exceptional G protein bias. To decode the underlying mechanism, we determined the cryo-EM structures of μOR bound to *(R)*-**141** in complex with Gi and with GRK2. Our structural, functional and dynamics data together reveal that *(R)*-**141** achieves this selectivity through a stepwise gating mechanism, in which the conformational dynamics of TM7 serves as a terminal checkpoint. This "conformational veto" by TM7 provides a mechanism to modulate β-arrestin recruitment at the final step. Collectively, our work provides a systemic vision of transducer selectivity and a framework for rational biased drug design.

Introduction

G protein-coupled receptors (GPCRs) represent the largest transmembrane receptor family. They respond to diverse extracellular signals and orchestrate intracellular signaling cascade[1]. Consequently, GPCRs represent the targets of more than 36% FDA-approved drugs[2]. Canonically, GPCR signaling involves two primary pathways: the G protein pathway and the β-arrestin pathway. These key transducers, heterotrimeric G proteins and β-arrestins, often compete for overlapping binding sites on the intracellular face of activated receptors, yet elicit distinct cellular response[3]. This functional divergence has underscored the therapeutic potential of biased agonists (or functionally selective agonists), which preferentially activate one pathway over the other, fueling intense interest in their development across the GPCR superfamily[4].

The μ-opioid receptor (μOR), a prototypic Family A GPCR, serves as the primary drug target of opioid analgesics including morphine and fentanyl, which induce both the G protein signaling pathway and the β-arrestin signaling pathway upon activation[5]. The escalating abuse of opioid drugs have precipitated a profound global public health emergency. The massive societal and clinical impacts of this crisis are fundamentally driven by the severe adverse effects of conventional μ-opioid receptor agonists, including addiction, respiratory depression, tolerance, and profound dependency. Some of these side effects may be linked to the activation of β-arrestin signaling pathway, despite ongoing controversies[6-8]. Given μOR's critical physiological roles and therapeutic values, it has emerged a model receptor for investigating GPCR-transducer bias. Over the past decades, numerous G protein-biased agonists with diverse chemical scaffolds have been developed

to mitigate clinical risks and elucidate the structure-activity relationships (SAR) underlying GPCR-transducer selectivity. To date, 19 structures of μOR-Gi complexes bound to various agonists[9-16], as well as 2 μOR-β-arrestin1 complexes[17], have been determined. These snapshots, combined with studies on protein dynamics using nuclear magnetic resonance (NMR)[18-20], single-molecular FRET (smFRET)[21] and molecular dynamics (MD) simulation[20,22-24], have offered remarkable insights into how distinct agonists stabilize specific receptor conformations at the cytoplasmic face to favor coupling to either G proteins or β-arrestins.

However, while these advances have established a foundational framework for understanding transducer bias, they capture only an incomplete picture of the signaling landscape. In the native cellular environment, high-affinity β-arrestin recruitment is canonically viewed as a direct downstream consequence of receptor phosphorylation by G protein-coupled receptor kinases (GRKs)[3,25]. Within this "phosphorylation barcode" model[26,27], GRKs serve as the obligate gatekeepers that license β-arrestin binding (Fig. 1a). Consequently, deciphering the structural basis of the initial GRK engagement is a prerequisite for understanding the initiation of signaling bias. Yet, emerging functional evidence indicates a profound uncoupling between kinase engagement and β-arrestin recruitment that challenges the sufficiency of this model. Strikingly, despite exhibiting a stronger ability to engage GRK2, the agonist fentanyl recruits less β-arrestin compared to DAMGO[28]. This disparity, coupled with the known requirement of receptor core interactions for β-arrestin activation[29], suggests that while GRK-mediated priming is a central regulatory event, it is mechanistically insufficient to independently dictate the final transducer transition. These observations imply the existence of an intrinsic conformational checkpoint within the receptor that operates in concert with the GRK machinery to filter downstream signals. Identifying this elusive regulatory element, which fine-tunes the complex triad of G protein, GRK, and β-arrestin interactions, is therefore essential for unraveling the complete structural basis of biased signaling.

In this study, we identified *(R)*-**141**, a novel μOR partial agonist that exhibits a pronounced G protein bias characterized by minimal GRK engagement and undetectable β-arrestin recruitment. To decode the structural basis of this atypical pharmacological profile and uncover the molecular determinants of transducer selectivity, we determined the cryo-EM structures of the *(R)*-**141**-bound μOR in complex with both Gi and GRK2. Integrating these structural insights with molecular dynamics (MD) simulations, we demonstrate that while GRK-induced receptor phosphorylation is a key regulatory event, it is not the sole determinant of β-arrestin binding. Instead, our findings

reveal that the intracellular terminus of TM7 acts as a critical conformational macro-switch, capable of preventing β-arrestin recruitment through a "conformational veto" mechanism. Specifically, the binding of *(R)*-**141** triggers a conformational cascade along a vertical signaling motif in TM7, stabilizing a receptor state that is structurally incompatible with productive β-arrestin engagement. Taken together, these findings redefine the structural paradigm of GPCR transducer selectivity, highlighting how the conformational integrity of TM7 provides a rational blueprint for the design of next-generation, biased GPCR modulators.

Identify μOR agonists with novel chemotypes through in silico screening

While the rational design of biased μOR agonists is impeded by a lack of structural clarity, the discovery of ligands with novel chemotypes holds the potential to exhibit unique signaling signatures and illuminate new mechanisms of bias[30]. Thus, we aimed to find μOR agonists with new chemotypes using high-throughput virtually screening. We docked about 4.3 million commercially available compounds into the orthosteric ligand pocket of the high-resolution active-state μOR structure (PDB ID: 5C1M) by Schrödinger[31] (see methods for details, Fig. 1b). After docking and filtering, top-ranked compounds were manually inspected based on their chemotype novelty and interaction with the surrounding residues, especially $D^{3.32}$, $Y^{7.43}$, and $H^{6.52}$ which are conservatively involved in interaction with other opioids[9,11-13,32,33], for further experimental validation.

After the first round of docking, we selected and validated 28 compounds using GTP-turnover assay and isotopic ligand competition binding assay. Of the compounds that compete with ^{3}H-diprenorphine, **64** exhibited promising agonist-like activity in the GTP-turnover assay (Fig.1c, Extended Data Fig.1 a-b). More importantly, the chemotype of **64** is different from any known μOR agonists (Extended Data Fig.1c). To take advantages of its chemotypes novelty and to improve the function, we conducted two rounds of analog screening for over 1.2 billion compounds followed by docking, aiming to identify **64** analogs with enhanced potency. During *in vitro* validation, we prioritized high-affinity compounds with partial efficacy. This selection was based on the empirical observation that reduced efficacy often correlates with diminished β-arrestin recruitment and larger therapeutic window, although the structural basis linking these functional attributes to specific receptor conformational dynamics remains elusive[21,28]. Finally, **141**, a partial agonist with novel chemotypes that bound to μOR at sub-μM affinity (IC_{50} is about 0.5 μM) was selected as initial hit compound for further studies. (Fig. 1c-e)

Pharmacological profile of *(R)*-141

The compound **141** used for the initial validation was a racemic mixture, containing a single stereocenter at the piperidine moiety (Extended Data Fig.1d). To resolve the stereochemistry, we synthesized two enantiomers (Extended Data Fig.1e, see methods for details) and evaluated their functional profiles by NanoBiT-based G_i protein dissociation assay. The results indicated that *(R)*-**141** exhibited higher potency and lower efficacy compared to the *(S)*-**141** (Extended Data Fig.1f), consistent with our strategy to prioritize partial agonists for minimizing β-arrestin recruitment, *(R)*-**141** was selected for further investigation.

To map the comprehensive signaling landscape of *(R)*-**141**, we quantified its activity across the canonical Gi, GRK2, and β-arrestin pathways using NanoBiT-based assays[34] (Fig. 1f-g). To rigorously define its signaling bias, we benchmarked *(R)*-**141** against a diverse panel of well-known μOR agonists, including the balanced agonist DAMGO, the first FDA-approved μOR biased agonist Oliceridine[35] and the plant-derived mitragynine pseudoindoxyl (MP)[11,36]. On the Gi protein dissociation assay, *(R)*-**141** behaved as a partial agonist, exhibiting ~40% efficacy relative to DAMGO and an EC_{50} of approximately 30 nM (Fig. 1f, left), consistent with our initial screening. Remarkably, while *(R)*-**141** maintained similar potency for GRK2 engagement compared to DAMGO, its maximal efficacy (E_{max}) was severely limited, reaching less than 10% of the DAMGO-induced response (Fig. 1f, right). Strikingly, *(R)*-**141** exhibited undetectable β-arrestin recruitment (Fig. 1g), even when GRK2 was overexpressed in the cells. The drastically reduced intrinsic efficacy for GRK2 engagement likely contributed to the undetectable β-arrestin recruitment of *(R)*-**141**, as GRK-induced μOR phosphorylation is a prerequisite for β-arrestin recruitment[3]. Our *in vitro* phosphorylation assays further support this mechanism, indicating insufficient μOR phosphorylation upon activation by *(R)*-**141 (**Extended Data Fig.2**)**. Notably, under identical experimental conditions, MP, previously reported as a highly G protein-biased agonist[11], still retained measurable β-arrestin recruitment activity (~10% of DAMGO Emax, Fig. 1g). This atypical pharmacological profile positions *(R)*-**141** as a promising lead compound for the development of next-generation analgesics with a wider therapeutic window.

(R)-141 exhibits promising therapeutic potential

Encouraged by the unique biased signaling profile observed *in vitro*, we next sought to evaluate whether *(R)*-**141** could translate these molecular advantages into a superior therapeutic value *in vivo*. Pharmacokinetic measurements demonstrate that *(R)*-**141** penetrates the blood-brain barrier

efficiently following administration, especially for the intraperitoneal administration (i.p., Extended Data Fig.1g). Meanwhile, *(R)*-**141** also exhibits subtype-selective activation on μOR compared to δOR and κOR (Extended Data Fig.1h). To evaluate its analgesic potential, a formalin injection assay was firstly used to compare the analgesic effects of *(R)*-**141** with those of morphine. The *in vivo* results suggest that *(R)*-**141** exhibits analgesia effects at relatively low doses (1 mg/kg in Phase I and 2.5 mg/kg in Phase II), whereas morphine at 5 mg/kg shows only modest analgesic effects (Fig. 1h).

We further evaluated whether *(R)*-**141** exhibits less severe side effects than morphine, particularly in terms of respiratory depression and constipation, which are known to limit the dosing of classical opioid analgesics. Morphine at a subtherapeutic dose (5 mg/kg) significantly inhibited the respiratory frequency, whereas 2.5 mg/kg of *(R)*-**141** induced minimal respiratory depression, as assessed by whole-body plethysmography (WBP). Although higher doses of *(R)*-**141** did cause some respiratory depression, the effect was transient, with recovery occurring shortly thereafter (Fig. 1j). Additionally, the assessment of total accumulated fecal boli indicates that *(R)*-**141** has no detectable effect on defecation (Fig.1k).

Collectively, *(R)*-**141** exhibits analgesic effects at relatively low doses while inducing fewer opioid-related side effects compared to morphine, notably in both respiratory depression and constipation. Despite having a limited maximum analgesic efficacy (MPE), *(R)*-**141** still offers a promising foundation for further optimization. The scaffold of the compound holds significant potential for advancing the development of novel opioid analgesics with improved therapeutic profiles.

Structural investigation of *(R)*-141 stabilized μOR-Gi and μOR-GRK2 complexes

Partial agonists of μOR with low intrinsic efficacy have long been considered to possess safer therapeutic profiles[28]. Indeed, our *in vitro* and *in vivo* studies demonstrate that *(R)*-**141** exhibits an atypical pharmacological profile and represents a promising scaffold for next-generation opioid analgesics. However, the structural basis by which partial agonism is coupled to precise transducer selectivity, and ultimately to clinical safety, remains poorly understood. In this context, partial agonists such as *(R)*-**141** offer unique chemical probes to dissect the subtle conformational landscapes that differentiate transducer engagement[21,37,38]. While numerous structures of μOR-Gi complexes and two μOR-β-arrestin complexes have been resolved, the critical μOR-GRK interface is missing, limiting our ability to dissect how partial agonism translates into biased signaling. To bridge this gap and exploit the unique properties of *(R)*-**141**, we determined the cryo-EM structures

of the *(R)*-**141**-bound μOR in complex with Gi, alongside the long-sought structure of the μOR-GRK2 complex.

Inspired by previous research, miniG_i protein was fused to the C terminus of μOR to facilitate the formation of μOR-G_i complex [39,40] (Extended Data Fig.3a). In contrast, for the μOR-GRK2-*(R)*-**141** structure, a NanoBiT-tethering strategy was employed to enhance the stability of the complex[41]. Both the μOR-Gi-*(R)*-**141**-scFv16 and μOR-GRK2-*(R)*-**141** complexes were purified and prepared for cryo-EM analysis (Extended Data Fig.3b-c and Extended Data Fig.4a; see methods for details). Subsequent data collection and processing yielded structures with a final resolution of 3.08 Å for both complexes (Extended Data Fig.3d-i and Extended Data Fig.4b-g; see methods for details). The high-quality electron density maps enabled the unambiguous modeling of most complex components, with the exception of the flexible RH domain of GRK2 (Fig. 2a-b).

The structures indicate *(R)*-**141** is in a very similar conformation in both Gi and GRK2-bound μOR structures, occupying the orthosteric pocket of μOR (Fig. 2c). Given this high structural similarity, we will primarily describe the specific ligand-receptor interactions using the μOR-Gi complex structure as a representative model. The phenol group of *(R)*-**141** packs against the hydrophobic side chain of $V^{5.42}$ (Fig. 3C). Consistent with this binding mode, alanine substitution of $V^{5.42}$ reduced the activation efficacy of *(R)*-**141**. (Fig. 2d). The different cell surface expression levels of the wild-type and each mutant were measured and are shown in Extended Data Fig.3j. According to previous research, a water-mediated hydrogen bond network between the ligand and $H^{6.52}$ and/or $K^{5.39}$ contribute to the function of opioids[33]. Due to the limitation of local density quality, we could not build the possible water molecules around the *(R)*-**141**. The $K^{5.39}$A mutation sightly affects the activation of *(R)*-**141** while $H^{6.52}$A influenced both the EC_{50} and Emax of *(R)*-**141**, suggesting their roles in interacting with *(R)*-**141** (Fig. 2d and Extended Data Fig.3j). A salt bridge between $D^{3.32}$ and a protonated amine group of the ligand is highly conserved for the μOR[33,42]. In the structure of μOR bound with *(R)*-**141**, instead of forming a salt bridge, a nitrogen atom at the linker region of *(R)*-**141** formed a hydrogen bond network with $D^{3.32}$ and $Y^{7.43}$(Fig. 2c). Mutagenesis studies indicated $D^{3.32}$ and $Y^{7.43}$ directly contributes to the function of *(R)*-**141** (Fig. 2d and Extended Data Fig.3j). Besides, the 2-ethylpyridine of *(R)*-**141** inserted into the cleft of TM2 and TM3, and contacted with $V^{3.28}$ (Fig. 2c), this hydrophobic interaction is crucial for the function of *(R)*-**141**, as $V^{3.28}$A mutation almost abolished the activation of *(R)*-**141** (Fig. 2d and Extended Data Fig.3j).

Prior to this study, structural insights into GPCR-GRK interactions were limited to the complexes of rhodopsin with GRK1[43] (Rho*-GRK1; PDB ID: 7MT8) and the neurotensin receptor with GRK2[41] (NTSR1-GRK2; PDB ID: 8JPB). While the μOR in our structure shares the hallmark outward displacement of TM6 seen in both Rho* and NTSR1 (Extended Data Fig.5a-b), our comparative analysis reveals distinct conformational features. Unlike GRK1, which undergoes a notable twist in its kinase domain when bound to Rho* (Extended Data Fig.5a), GRK2 maintains a largely conserved overall conformation when complexed with either NTSR1 or μOR (Extended Data Fig.5b). However, a closer analysis highlights striking differences in the receptor-transducer interface. Specifically, the μOR exhibits a more outward tilted conformation of TM6 (the distance between TM4 and TM6 terminus is 39 Å, determined by the distance between Cα atoms of $R^{4.40}$ and $K^{6.24}$, Extended Data Fig.5c) compared to NTSR1 (the distance between TM4 and TM6 terminus is 36 Å, determined by the distance between Cα atoms of $S^{4.40}$ and $P^{6.24}$, Extended Data Fig.5c). However, GRK2 engages the μOR at a lower position relative to NTSR1, with a downward shift of approximately 3.9 Å (determined by the distance between Cα atoms of L4 in two structures, Extended Data Fig.5d). Unlike NTSR1, which engages GRK2 primarily via ICL2, TM6, and Helix 8, the μOR interacts with GRK2 mainly through ICL3, TM6, and Helix 8 (Fig. 2e and Extended Data Fig.5e). $N^{8.49}$ directly interacts with E5 of GRK2. The $N^{8.49}$A mutation completely abolished *(R)*-**141** induced GRK2 engagement and substantially impaired DAMGO induced GRK2 recruitment. Among the three positively charged residues oriented toward the αN helix of GRK2 ($R265^{ICL3}$, $R^{6.28}$, $R^{6.32}$), only the $R^{6.32}$A mutation exhibited pronounced effects on GRK2 recruitment (Fig. 2e-f, Extended Data Fig.3j). Although no direct interaction between $R^{6.32}$ and GRK2 was observed in the structure, an indirect interaction mediated by unresolved water molecules is likely. Interestingly, both the $R^{6.32}$A and $N^{8.49}$A mutations had a greater effect on *(R)*-**141** mediated GRK2 recruitment than on that induced by DAMGO (Fig. 2f, Extended Data Fig.3j), suggesting that DAMGO may stabilize a μOR-GRK2 complex conformation distinct from the one induced by *(R)*-**141**. In these divergent states, $R^{6.32}$ and $N^{8.49}$ may adopt different orientations, contributing differentially to the stability of the respective signaling complexes. Furthermore, the large lobe and PH domain of GRK2 undergo subtle but distinct rotations to accommodate this interface (Extended Data Fig.5d). Together, these findings expand the structural landscape of GPCR regulation, providing comprehensive insights into both the conserved and receptor-specific modes of GRK engagement.

Decoupling GRK engagement and β-arrestin recruitment

Capturing the pivotal intermediate link between G protein activation and β-arrestin recruitment, the μOR-GRK2-*(R)*-**141** structure supplies a crucial piece of the puzzle in the structural cycle of GPCR-transducer interaction (Fig. 1a). With the full set of transducer complexes now available, we can rigorously define the atomic determinants that drive the receptor's selectivity between distinct transducers, particularly for GRK2, which acts as the initial gatekeeper regulating the switch from G protein to β-arrestin signaling.

Structural alignment of the μOR in complex with different ligands and transducers reveals that the receptor maintains a largely conserved active conformation, with the notable exception of subtle differences at the intracellular half of TM7 and Helix 8 (Fig. 3a). Specifically, we observed that *(R)*-**141** stabilizes an inward shift of TM7 and Helix 8 in both the Gi- and GRK2-bound structures. In contrast, this feature is absent in the DAMGO-bound μOR-Gi and μOR-β-arrestin complexes (Fig. 3a). Furthermore, this *(R)*-**141**-induced inward conformation facilitates the formation of an ionic lock between $R^{3.50}$ (of the conserved D/ERY motif) and $D^{8.47}$, located directly above the transducer-binding pocket (Fig. 3b-c). In the DAMGO-bound state as well as other agonist-stabilized μOR-Gi complexes, this $R^{3.50}$-$D^{8.47}$ interaction is absent due to insufficient proximity and/or unfavorable side-chain orientations (Fig. 3d-e and Extended Data Fig.6).

The striking correlation between the presence of the $R^{3.50}$-$D^{8.47}$ ionic lock and the atypical pharmacological profile of *(R)*-**141** suggests that this interaction may function as a structural anchor for transducer selectivity. Notably, R3.50 resides within the conserved 'D/ERY' motif, which plays pivotal roles in GPCR signaling [44]. To evaluate the functional impact of this ionic lock on the pharmacological landscape of the μOR, we performed targeted mutagenesis at the $D^{8.47}$ position. We exchanged this residue with either asparagine ($D^{8.47}$N) to disrupt the potential for ionic lock formation or glutamic acid ($D^{8.47}$E) to promote the interaction, by elongating the acidic side chain by one methyl group that allows the ionic lock to be formed even at longer distances. While both $D^{8.47}$N and $D^{8.47}$E maintained the capacity to activate G protein signaling upon DAMGO stimulation (~ 50% decrease compared to wild type receptor, Fig. 3f and Extended Data Fig.3j), their effects on GRK engagement were markedly different. The $D^{8.47}$E mutation significantly reduced the ability of DAMGO to recruit GRK2, whereas $D^{8.47}$N exhibited GRK engagement comparable to the wild-type receptor (Fig. 3g and Extended Data Fig.3j).

These observations are consistent with the minimal GRK engagement observed for *(R)*-**141.** In the μOR-GRK2-*(R)*-**141** complex, the αN helix of GRK2 engages at a shallower depth (~3.9 Å)

compared to the full agonist-bound NTSR1-GRK2 complex[41] (Extended Data Fig.5d). Superposition of the receptor parts in the two structures reveals that accommodating the GRK2 αN helix at a comparable depth would result in a severe steric clash with μOR helix 8 (Extended Data Fig.5f-h). These structural superpositions suggest a plausible model that in the presence of GRK, the $R^{3.50}$-$D^{8.47}$ ionic lock promoted by *(R)*-**141** effectively restrains the volume of the μOR intracellular pocket, thereby precluding the deeper αN insertion required for effective GRK engagement in full-agonist states. In contrast, DAMGO appears to preclude the formation of this lock, leaving the intracellular cavity accessible for deeper insertion of the GRK2 αN helix (Extended Data Fig.5i). Consequently, the $D^{8.47}$E substitution may mimic the intracellular restraint observed in the μOR-GRK2-*(R)*-**141** complex, thereby reducing the efficiency of GRK2 recruitment for DAMGO (Fig. 3g). Notably, structural measurements confirm that $D^{8.47}$ is not directly involved in the transducer interaction. The closest inter-atomic distances between $D^{8.47}$ and the respective effectors are 8.7 Å for GRK2 (measured from $D^{8.47}$ OD1 to L4 CD2, Extended Data Fig.5j), and 4.6-4.7 Å for β-arrestin1 (measured from $D^{8.47}$ OD1 to D69 Cα in PDB IDs 9WSX and 9WSV, Extended Data Fig.5k-l). These distances preclude the formation of direct salt bridges or strong hydrogen bonds with the transducers.

The most consequential finding arises from the diametrically opposed β-arrestin recruitment profiles of the two $D^{8.47}$ mutants, which effectively decouple GRK2 engagement from downstream signaling. Strikingly, while the $D^{8.47}$N substitution maintains GRK2 engagement levels comparable to the wild-type receptor upon DAMGO activation, it almost completely abolishes β-arrestin recruitment. Conversely, although the $D^{8.47}$E mutation significantly impairs the recruitment of GRK2, it unexpectedly preserves the receptor's ability to recruit β-arrestin (~ 50% decrease compared to wild type receptor, Fig. 3f). Of note, the parallel assessment within the $D^{8.47}$N/E mutant ensures that the observed changes in transducer selectivity are independent of its surface expression levels.

This mirror-image paradox, where β-arrestin signaling is either silenced despite GRK binding or maintained despite GRK deficiency (Fig.3f-g and Extended Data Fig.3j), directly challenges the linear model of transducer recruitment of GPCR, providing compelling evidence for a second gating mechanism that governs the GPCR-β-arrestin interaction. Specifically, we observed that while DAMGO induced a similar low level of GRK2 engagement for the $D^{8.47}$E mutant as *(R)*-**141** for the wild-type μOR (both reaching only ~10% of the GRK2 recruitment seen with DAMGO-WT,

Fig. 3f, Fig. 1f and Extended Data Fig.3j) the $D^{8.47}E$ mutant still maintained approximately 50% of the β-arrestin recruitment, whereas recruitment by *(R)*-**141** remained completely undetectable (Fig.3f, Fig.1g and Extended Data Fig.3j). This profound decoupling between GRK2 engagement and β-arrestin recruitment indicates that *(R)*-**141** triggers an additional mechanism that directly prevents the β-arrestin interaction, independent of the upstream GRK2 engagement.

The conformational dynamics of TM7 and transducer selectivity

To identify such an additional mechanism that governs the transducer selectivity of the μOR, we performed MD simulations of the receptor bound to either *(R)*-**141** or DAMGO in a transducer-free state. By examining the receptor's conformational landscape in a state equally accessible to G proteins, GRKs, and β-arrestins, we aimed to transition from static structural snapshots to a dynamic understanding of the receptor.

We performed 15 independent 3.5μs simulations for both DAMGO bound and *(R)*-**141** bound μOR systems to monitor the dynamics of the receptor in the absence of intracellular signaling proteins (see Methods). The MD simulations revealed striking differences in the dynamics of the TM7 intracellular segment, monitored by the orientation of $F^{7.55}$. In *(R)*-**141** and DAMGO-bound μOR-Gi structures, as well as μOR-β-arrestin1-DAMGO structure, $F^{7.55}$ is initially positioned toward a pocket flanked by Helix 8 and TM1 (Extended Data Fig.7, note that this side chain lacks defined electron density. Our simulations show that in both *(R)*-**141** and DAMGO-bound states, the TM7 terminus undergoes a counter-clockwise rotation (viewed from the intracellular side, Fig. 4a, left), a movement that is intrinsically coupled with the flipping of $F^{7.55}$ out of its initial position towards TM6 and more into the center of the TM7 bundle (Fig. 4a, left, Supplementary Figure 1-2). As $F^{7.55}$ settles into an orientation vertical to the axis of Helix 8, the local secondary structure of the TM7 terminus is simultaneously reshaped. Before the flipping of $F^{7.55}$, a main-chain hydrogen bond between the oxygen of $P^{7.50}$ and the nitrogen of $F^{7.55}$ stabilizes a characteristic π-bulge at $Y^{7.53}$, maintaining this segment in a π-helical conformation (Fig. 4a, middle). Upon the flipping of $F^{7.55}$, this interaction is replaced by a new hydrogen bond between the oxygen of $P^{7.50}$ and nitrogen of $A^{7.54}$ (Fig.4a, right). Consequently, the π-bulge at $Y^{7.53}$ is released, and this segment relaxes into a canonical α-helix (Fig. 4a). Notably, while this conformational transition occurs in both systems, the $F^{7.55}$ flip and subsequent straightening of the TM7 proceed more rapidly in the simulations of the *(R)*-**141**-bound receptor than in the DAMGO-bound receptor (Fig. 4a-b).

Analysis of the MD trajectories revealed that this π-bulge release is temporally coupled to the rotation of $F^{7.55}$ out of a hydrophobic pocket formed by residues in TM1 ($G^{1.49}$, $L^{1.52}$, and $V^{1.53}$), TM7 ($P^{7.50}$), and Helix 8 ($F^{8.50}$ and $F^{8.54}$) (Fig. 4c). To prove, whether the different dynamic dwell times of the TM7 π-helical conformation, observed for both *(R)*-**141** and DAMGO (Supplementary Figure.1-2), serve as a determinant of transducer selectivity, we performed site-directed mutagenesis in combination with functional assays. To accelerate this conformational transition and investigate the influence of π-to-α helix transition to transducer selectivity of receptor, we mutated $F^{7.55}$ to alanine ($F^{7.55}A$) and assessed the resulting signaling profile. Functional profiling of this mutation reveals a striking decoupling of downstream signaling pathways. Remarkably, while the mutation exhibits negligible effects on G protein activation and GRK recruitment, it completely abrogated DAMGO-stimulated β-arrestin engagement (Fig. 4d). These data collectively imply that the transition of TM7 to an α-helical conformation imposes a structural barrier against β-arrestin coupling.

Additionally, a recent structural study of the μOR-β-arrestin1 complex reported that the polar interactions between $N^{1.50}$-$S^{7.46}$ and $D^{2.50}$-$N^{7.49}$ are important for β-arrestin1 recruitment (18). Consistently, our MD simulations reveal a tight temporal coupling between the loss of these essential interactions and the collapse of the TM7 π-helical conformation (Extended Data Fig.8, Supplementary Figure.3-4). The π-to-α helix transition inherently dismantles these critical interactions in real-time, serving as a structural rationale for how the α-helical state precludes β-arrestin engagement.

Molecular mechanism underlying the TM7 conformational dynamics modulated by *(R)*-141

Although our preceding structural and functional results establish intracellular TM7 dynamics as a determinant of μOR transducer selectivity, how extracellular binding of *(R)*-**141** drives the rapid conformational transition remains unclear. To bridge this spatial gap, we next investigated the allosteric communication network that propagates the ligand-induced signal across the transmembrane domain to facilitate the π-to-α straightening of TM7.

Correlated with the straightening of TM7, we observe disruption of the water-mediated $N^{7.45}$-$N^{7.49}$-$Y^{7.53}$ hydrogen bond network in the transmembrane core of μOR (Fig. 5a). Temporally, trajectory analyses reveal that the collapse of this water network is strictly coupled with the release of the π-bulge, demonstrating a tight temporal and structural coupling between these two events (Supplementary Figure. 5-6). Faster disruption of this central network connecting extra and intracellular receptor regions, is reflected by a lower average water occupancy within this network in

the *(R)*-**141**-bound compared to the DAMGO-bound receptor simulations (Fig. 5b). Given the proposed central role of this network in signal transfer between the ligand-binding pocket and the transducer-coupling region (32), this synchronized dynamic offers a compelling structural framework for elucidating its impact on the transducer selectivity of the μOR.

We hypothesized that stabilizing the water-mediated hydrogen-bonding network would restore β-arrestin recruitment in response to *(R)*-**141**, whereas perturbing it would abolish DAMGO-induced β-arrestin coupling. To structurally reinforce the water-mediated hydrogen-bonding network, we introduced the $N^{7.45}Q$ mutation (Fig. 5a). We reasoned that the extended γ-carboxamide side chain of glutamine, gaining increased conformational flexibility, could reach deeper into the polar core, thereby strengthening local hydrogen-bonding interactions. Indeed, analysis of 15 independent 3.5μs MD simulations of *(R)*-**141** bound receptor confirmed that the $N^{7.45}Q$ mutant maintained a more robust water network between $Q^{7.45}$ and $Y^{7.53}$ (Supplementary Figure.7). This enhanced polar core stability directly correlated with a delayed release of the TM7 π-bulge compared to the wild-type simulations (Fig. 5c and Supplementary Figure.7). Consistently, while this mutation had minimal impact on G protein activation in response to *(R)*-**141** (Fig. 5d, left) it enhanced GRK2 engagement (Fig. 5d, middle) and restored β-arrestin recruitment (Fig.5d, right). In contrast, the $Y^{7.53}F$ mutation disrupted the water-mediated network and facilitated straightening of TM7 in 15 independent 3.5μs MD simulations of DAMGO bound receptor (Fig.5e and Supplementary Figure.11). While this mutation clearly reduced G protein activation (~50%, Fig.5f, left), it only slightly reduced GRK2 engagement (~80% of wild-type level, Fig.5f, middle) but completely abolished β-arrestin recruitment (Fig.5f, right).

Notably, the $N^{7.49}A$ mutation that targets the highly conserved $N^{7.49}$ within the NPxxY motif, a central residue of the water-mediated network, severely impaired μOR interactions with all tested transducers (Extended Data Fig.9). Together, these data highlight the $N^{7.45}$-$N^{7.49}$-$Y^{7.53}$ core as the critical mechanistic hub for transducer preference. The intrinsic stability of this water-mediated network modulates the dwell time of the TM7 π-bulge release, which in turn orchestrates the sequential coupling of different transducers.

Having established the central water network as the allosteric hub for intracellular TM7 dynamics, a fundamental question arises: how does the binding of *(R)*-**141** within the orthosteric pocket propagate an allosteric signal to destabilize this core and drive the subsequent conformational change? Temporally synchronized with the rearrangement of the water-mediated $N^{7.45}$-$N^{7.49}$-$Y^{7.53}$

network and the release of the π-bulge, we observed a distinct tightening of the helical segment bridging the ligand-binding pocket and $N^{7.45}$. This helical compaction is quantitatively reflected by a reduced backbone hydrogen bond distance between $L^{7.41}$ and $N^{7.45}$ (Fig. 5g-h and Supplementary Figure.8-11). More specifically, the dwell time of this helical tightening are highly tunable: the process was significantly delayed in the $N^{7.45}$Q mutant (for *(R)*-**141**, compared to wild-type; Fig. 5h and Supplementary Figure.8-11) and markedly accelerated in the $Y^{7.53}$F mutant (for DAMGO, compared to wild-type; Fig. 5h and Supplementary Figure.8-11). Strikingly, these distinct structural profiles nicely correlate with the observed pharmacological phenotypes of the two mutants (Fig. 5d and f).

Structurally, this helical compaction is related to the movement of $Y^{7.43}$ (Fig. 5i), which engages *(R)*-**141** through a polar network comprising $D^{3.32}$, $Y^{7.43}$, and $Q^{2.60}$ (Fig. 5j). Therefore, this localized helical compaction may serve as the critical mechanical bridge linking the initial ligand recognition to the divergent downstream conformational dynamics. Furthermore, $Y^{7.43}$ appears to play an important role in the functional response of the μOR to different agonists; the $Y^{7.43}$F substitution significantly impairs the G protein signaling induced by MP, DAMGO, lofentanil (12), and *(R)*-**141** (Fig. 2d).

In summary, our data reveal that TM7 functions as an intrinsic allosteric macro-switch that modulates the transducer selectivity of the μOR. This switch is operated through a vertical signaling axis we designate as the "pYN motif" (palindromic $Y^{7.43}$-$N^{7.45}$-$N^{7.49}$-$Y^{7.53}$, Fig. 5k). *(R)*-**141** toggles this cascade by engaging $Y^{7.43}$ in the ligand binding pocket, modulating the central water network, and subsequently stabilizing the TM7 intracellular terminus into a state hindering β-arrestin recruitment. This intrinsic "conformational veto" operates as a terminal checkpoint at the intracellular interface (Fig.6). It refines the canonical view of the GRK-β-arrestin axis by framing transducer selectivity as a stepwise, multi-layered process, while GRK-mediated phosphorylation may serve as an initial permit, the conformational status of the receptor core acts as a terminal structural gate. Even if prior upstream events occur normally, this mechanism dictates the ultimate signaling outcome by precluding β-arrestin recruitment, thereby ensuring signaling fidelity and precision.

Discussion

Biased signaling of GPCRs has been considered a significant opportunity to mitigate on-target side effects associated with GPCR-targeted therapies and has been the focus of intensive research

for many years[4,45]. Biased agonists targeting various GPCR subtypes, including adrenergic receptors, opioid receptors, dopamine receptors, chemokine receptors, and angiotensin receptors, have been developed, with several already approved for clinical use[4]. However, a deeper and more systematic understanding of GPCR-transducer selectivity is needed to drive biased drug innovation. Previous research has modeled GPCRs as dynamic allosteric proteins that adopt distinct conformations when bound to various agonists. Agonist-induced conformational changes initiate at the extracellular orthosteric pocket and propagate along the transmembrane domain. The highly dynamic properties and intricate cross-communications between the ligand-binding pocket and the transducer-binding pocket make investigations into biased agonism particularly challenging[46].

In this study, we identified *(R)*-**141** as a novel G protein-biased agonist of μOR. Despite the reported development of numerous biased ligands, including Oliceridine[35] and MP[36], they still exhibit some degree of β-arrestin recruitment in the presence of GRK (Fig. 1f-g). This closely intertwined phenomenon hinders a comprehensive understanding of transducer selectivity of GPCR. Therefore, *(R)*-**141**, with its noncanonical pharmacological profile and novel chemical scaffold, serves as an ideal probe to structurally decouple these convoluted signaling cascades, thereby providing more informative insights into the structural basis of biased agonism. For decades, GRK-mediated phosphorylation has been established as a canonical prerequisite for β-arrestin recruitment. Extensive research has been dedicated to decoding how the "phosphorylation barcode" induced by various agonists dictates the interaction between the receptor and β-arrestin[26,27]. Parallel to these findings, structural and dynamic studies have demonstrated that GPCRs can be stabilized into discrete conformational states that preferentially favor either G protein or β-arrestin coupling[20,21]. While these disparate lines of inquiry have provided profound insights into transducer selectivity, they often lack a cohesive, systemic vision of how the GRK machinery and the receptor's intrinsic conformational landscape cooperatively determine the final signaling output during the transition from G protein signaling to β-arrestin signaling.

By leveraging the unique pharmacological properties of *(R)*-**141**, we systematically dissected the structural determinants of transducer selectivity, establishing a comprehensive framework that integrates G protein activation, GRK engagement, and β-arrestin recruitment. We elucidate that the profound bias of *(R)*-**141** is achieved through a stepwise gating mechanism. The first checkpoint involves the modulation of GRK-mediated receptor phosphorylation. Specifically, *(R)*-**141**

promotes the formation of a $R^{3.50}$-$D^{8.47}$ ionic lock (Fig. 3b), which effectively constrains the intracellular pocket and reduces GRK2 engagement. Consistently, targeted mutations designed to facilitate this lock (e.g., $D^{8.47}E$) were sufficient to abrogate GRK recruitment by the full agonist DAMGO (Fig. 3g). However, this initial gating step alone is insufficient to completely prevent β-arrestin recruitment. This is clearly illustrated by the pharmacological profile of the μOR $D^{8.47}E$ mutant: despite having less than 10% of the wild-type's capacity for GRK engagement, a level comparable to the minimal GRK recruitment observed for *(R)*-**141**, this mutant still effectively recruits β-arrestin (Fig. 1f-g and Fig. 3f-h). This pivotal observation confirms that the reduction in GRK engagement at the first step is not the only determinant of biased signaling, necessitating the presence of a second, independent gating to fully prevent β-arrestin recruitment.

The decoupling of GRK2 recruitment from β-arrestin signaling in the $D^{8.47}$ mutants (for DAMGO) establishes the existence of a second, fail-safe gating mechanism within the μOR core. This ultimate checkpoint is defined by the conformational dynamics of TM7. Specifically, the rapid π-bulge release of TM7 into a straight α-helical conformation, induced by *(R)*-**141** in its transducer-free landscape, creates a structural environment that is intrinsically unfavorable for β-arrestin engagement. The fact that mimicking this fast π-bulge release (as seen in the $Y^{7.53}F$ and $F^{7.55}A$ mutant of DAMGO) selectively abolishes β-arrestin recruitment while leaving GRK2 engagement largely intact underscores the role of TM7 dynamics as a conformational veto. In this multi-layered framework, the $R^{3.50}$-$D^{8.47}$ ionic lock and the TM7 π-to-α transition function in concert to ensure robust signaling bias of *(R)*-**141**. Even if the initial phosphorylation barrier is bypassed, this secondary conformational gate serves as the ultimate safeguard, providing a terminal blockade that precludes productive β-arrestin recruitment. Crucially, this distinct dynamical signature is not restricted to the intracellular region. Rather, it reveals a profound long-range allosteric communication network extending from the orthosteric pocket (Fig. 5g-h) down to the transducer interface. Ligand engagement initiates a continuous conformational cascade that propagates through a vertical signaling axis along TM7 (Fig. 5k). This bidirectional allosteric conduit ensures that specific extracellular binding events are mechanistically coupled to intracellular conformational dynamics, thereby orchestrating precise transducer selectivity across the entire receptor architecture.

Importantly, our trajectory analyses show no direct temporal correlation between the formation of the $R^{3.50}$-$D^{8.47}$ ionic lock and the TM7 π-bulge release (Supplementary Figure.12-13), suggesting

that these two structural events constitute mechanistically decoupled regulatory axes. Consequently, the precise structural mechanism by which the $D^{8.47}N$ mutation independently abrogates β-arrestin recruitment remains an open question. Nevertheless, this orthogonal complexity does not compromise our central discovery. By definitively establishing the TM7 π-to-α transition as the primary ligand-driven gating, our study successfully decodes the allosteric conduit along TM7 and provide a clear, single-residue resolution blueprint explaining how the biased agonist *(R)*-**141** structurally enforces its profound signaling bias and dictates the exclusion of β-arrestin recruitment.

Traditionally, GPCRs are categorized based on their C-terminal affinity for β-arrestin into Class A ("transient", e.g., β_2AR and μOR) and Class B ("stable", e.g., V_2R and NTSR1)[47]. Class B receptors possess abundant phosphorylation sites that facilitate a stable "tail engagement" conformation, where the core engagement of the β-arrestin finger loop into the receptor cavity is often secondary or even unnecessary for recruitment[48]. In contrast, for Class A receptors like the μOR, stable recruitment is primarily driven by the "core engagement" mode[49], necessitating the deep insertion of the β-arrestin finger loop into the intracellular cavity of a GPCR, except for a recently discovered "pendulum conformation" stabilized by an allosteric modulator[50]. Given the immediate spatial proximity of TM7 to the β-arrestin finger loop, it is structurally mandated that the conformational state of this transmembrane helix should modulate the process of the recruitment. Previous studies also highlighted the role of TM7 in modulation transducer selectivity of GPCR[12,20,51]. Our study thus provides a robust molecular framework to explain how the receptor core, specifically the TM7-mediated conformational gate, functions as a critical structural determinant. This may ensure that for Class A receptors, where core engagement is indispensable under most physiological conditions, the conformational dynamics of the receptor itself provide an essential layer of transducer selectivity, and can even override, the canonical phosphorylation-dependent β-arrestin recruitment.

Taken together, starting with the identification of *(R)*-**141** as a pronounced G protein-biased agonist of μOR, our study provides a comprehensive structural framework for understanding GPCR-transducer selectivity. While the outward movement of TM6 has long been established as the universal hallmark of receptor activation, we systematically identify the TM7 as the decisive

macro-switch that governs transducer preference. By delineating these distinct structural determinants, our findings pave the way for rational, mechanism-based drug design for GPCR-related diseases.

References

1 Fredriksson, R., Lagerström, M. C., Lundin, L. G. & Schiöth, H. B. The G-protein-coupled receptors in the human genome form five main families. Phylogenetic analysis, paralogon groups, and fingerprints. *Mol Pharmacol* **63**, 1256–1272 (2003). https://doi.org/10.1124/mol.63.6.1256

2 Hutchings, C. J., Koglin, M., Olson, W. C. & Marshall, F. H. Opportunities for therapeutic antibodies directed at G-protein-coupled receptors. *Nat Rev Drug Discov* **16**, 787–810 (2017). https://doi.org/10.1038/nrd.2017.91

3 Weis, W. I. & Kobilka, B. K. The Molecular Basis of G Protein–Coupled Receptor Activation. *Annu Rev Biochem* **87**, 897–919 (2018). https://doi.org/10.1146/annurev-biochem-060614-033910

4 Smith, J. S., Lefkowitz, R. J. & Rajagopal, S. Biased signalling: from simple switches to allosteric microprocessors. *Nat Rev Drug Discov* **17**, 243–260 (2018). https://doi.org/10.1038/nrd.2017.229

5 Stein, C. Opioid Receptors. *Annu Rev Med* **67**, 1–19 (2014). https://doi.org/10.1146/annurev-med-062613-093100

6 Bohn, L. M., Gainetdinov, R. R., Lin, F.-T., Lefkowitz, R. J. & Caron, M. G. μ-Opioid receptor desensitization by β-arrestin-2 determines morphine tolerance but not dependence. *Nature* **408**, 720–723 (2000). https://doi.org/10.1038/35047086

7 Raehal, K. M., Walker, J. K. L. & Bohn, L. M. Morphine Side Effects in β-Arrestin 2 Knockout Mice. *J Pharmacol Exp Ther* **314**, 1195–1201 (2005). https://doi.org/10.1124/jpet.105.087254

8 Bachmutsky, I., Wei, X. P., Durand, A. & Yackle, K. ß-arrestin 2 germline knockout does not attenuate opioid respiratory depression. *Elife* **10**, e62552 (2021). https://doi.org/10.7554/elife.62552

9 Koehl, A. *et al.* Structure of the μ Opioid Receptor-Gi Protein Complex. *Nature* **558**, 547–552 (2018). https://doi.org/10.1038/s41586-018-0219-7

10 Gmeiner, P. *et al.* Structure-based Evolution of G protein-biased μ-opioid Receptor Agonists. *Angewandte Chemie Int Ed*, e202200269 (2022). https://doi.org/10.1002/anie.202200269

11 Qu, Q. *et al.* Insights into distinct signaling profiles of the μOR activated by diverse agonists. *Nat Chem Biol*, 1–8 (2022). https://doi.org/10.1038/s41589-022-01208-y

12 Zhuang, Y. *et al.* Molecular recognition of morphine and fentanyl by the human μ-opioid receptor. *Cell* **185**, 4361–4375.e4319 (2022). https://doi.org/10.1016/j.cell.2022.09.041

13 Wang, Y. *et al.* Structures of the entire human opioid receptor family. *Cell* (2023). https://doi.org/10.1016/j.cell.2022.12.026

14 Faouzi, A. *et al.* Structure-based design of bitopic ligands for the μ-opioid receptor. *Nature* **613**, 767–774 (2023). https://doi.org/10.1038/s41586-022-05588-y

15 Kaneko, S. *et al.* Structural and dynamic insights into the activation of the μ-opioid receptor by an allosteric modulator. *Nature Communications* **15**, 3544 (2024). https://doi.org/10.1038/s41467-024-47792-6

16 Ople, R. S. *et al.* Signaling Modulation Mediated by Ligand Water Interactions with the Sodium Site at μOR. *ACS Cent Sci* **10**, 1490–1503 (2024). https://doi.org/10.1021/acscentsci.4c00525

17 Zhang, H. *et al.* The molecular basis of μ-opioid receptor signaling plasticity. *Cell Res.*, 1–16 (2025). https://doi.org/10.1038/s41422-025-01191-8

18 Sounier, R. *et al.* Propagation of conformational changes during μ-opioid receptor activation. *Nature* **524**, 375–378 (2015). https://doi.org/10.1038/nature14680

19 Okude, J. *et al.* Identification of a Conformational Equilibrium That Determines the Efficacy and Functional Selectivity of the μ-Opioid Receptor. *Angew Chem Int Ed Engl* **54**, 15771–15776 (2015). https://doi.org/10.1002/anie.201508794

20 Cong, X. *et al.* Molecular insights into the biased signaling mechanism of the μ-opioid receptor. *Molecular Cell* **81**, 4165–4175.e4166 (2021). https://doi.org/10.1016/j.molcel.2021.07.033

21 Zhao, J. *et al.* Ligand efficacy modulates conformational dynamics of the μ-opioid receptor. *Nature* **629**, 474–480 (2024). https://doi.org/10.1038/s41586-024-07295-2

22 Kelly, B. *et al.* Delineating the Ligand–Receptor Interactions That Lead to Biased Signaling at the μ-Opioid Receptor. *J Chem Inf Model* **61**, 3696–3707 (2021). https://doi.org/10.1021/acs.jcim.1c00585

23 Kapoor, A., Martinez-Rosell, G., Provasi, D., de Fabritiis, G. & Filizola, M. Dynamic and Kinetic Elements of μ-Opioid Receptor Functional Selectivity. *Sci Rep* **7**, 11255 (2017). https://doi.org/10.1038/s41598-017-11483-8

24 Yuan, S. *et al.* The mechanism of ligand-induced activation or inhibition of μ- and κ-opioid receptors. *Angew Chem Int Ed Engl* **54**, 7560–7563 (2015). https://doi.org/10.1002/anie.201501742

25 Choi, M. *et al.* G protein-coupled receptor kinases (GRKs) orchestrate biased agonism at the β(2)-adrenergic receptor. *Sci Signal* **11** (2018). https://doi.org/10.1126/scisignal.aar7084

26 Liggett, S. B. Phosphorylation barcoding as a mechanism of directing GPCR signaling. *Sci Signal* **4**, pe36 (2011). https://doi.org/10.1126/scisignal.2002331

27 Miess, E. *et al.* Multisite phosphorylation is required for sustained interaction with GRKs and arrestins during rapid μ-opioid receptor desensitization. *Science Signaling* **11** (2018). https://doi.org/10.1126/scisignal.aas9609

28 Gillis, A. *et al.* Low intrinsic efficacy for G protein activation can explain the improved side effect profiles of new opioid agonists. *Science Signaling* **13** (2020). https://doi.org/10.1126/scisignal.aaz3140

29 Shiraishi, Y. *et al.* Biphasic activation of β-arrestin 1 upon interaction with a GPCR revealed by methyl-TROSY NMR. *Nature Communications* **12**, 7158 (2021). https://doi.org/10.1038/s41467-021-27482-3

30 Manglik, A. *et al.* Structure-based discovery of opioid analgesics with reduced side effects. *Nature* **537**, 185–190 (2016). https://doi.org/10.1038/nature19112

31 Halgren, T. A. *et al.* Glide: A New Approach for Rapid, Accurate Docking and Scoring. 2. Enrichment Factors in Database Screening. *Journal of Medicinal Chemistry* **47**, 1750–1759 (2004). https://doi.org/10.1021/jm030644s

32 Manglik, A. *et al.* Crystal structure of the μ-opioid receptor bound to a morphinan antagonist. *Nature* **485**, 321–326 (2012). https://doi.org/10.1038/nature10954

33 Huang, W. *et al.* Structural insights into μ-opioid receptor activation. *Nature* **524**, 315–321 (2015). https://doi.org/10.1038/nature14886

34 Inoue, A. *et al.* Illuminating G-Protein-Coupling Selectivity of GPCRs. *Cell* **177**, 1933–1947.e1925 (2019). https://doi.org/10.1016/j.cell.2019.04.044

35 Chen, X.-T. *et al.* Structure–Activity Relationships and Discovery of a G Protein Biased μ Opioid Receptor Ligand, [(3-Methoxythiophen-2-yl)methyl]({2-[(9R)-9-(pyridin-2-yl)-6-oxaspiro-[4.5]decan-9-yl]ethyl})amine (TRV130), for the Treatment of Acute Severe Pain. *Journal of Medicinal Chemistry* **56**, 8019–8031 (2013). https://doi.org/10.1021/jm4010829

36 Kruegel, A. C. *et al.* 7-Hydroxymitragynine Is an Active Metabolite of Mitragynine and a Key Mediator of Its Analgesic Effects. *ACS Central Science* **5**, 992–1001 (2019). https://doi.org/10.1021/acscentsci.9b00141

37 Wingler, L. M. *et al.* Angiotensin Analogs with Divergent Bias Stabilize Distinct Receptor Conformations. *Cell* **176**, 468–478.e411 (2019). https://doi.org/10.1016/j.cell.2018.12.005

38 West, G. M. *et al.* Ligand-dependent perturbation of the conformational ensemble for the GPCR β2 adrenergic receptor revealed by HDX. *Structure* **19**, 1424–1432 (2011). https://doi.org/10.1016/j.str.2011.08.001

39 Carpenter, B. & Tate, C. G. Engineering a minimal G protein to facilitate crystallisation of G protein-coupled receptors in their active conformation. *Protein Eng Des Sel* **29**, 583–594 (2016). https://doi.org/10.1093/protein/gzw049

40 Harris, J. A. *et al.* Selective G protein signaling driven by substance P–neurokinin receptor dynamics. *Nat Chem Biol* **18**, 109–115 (2022). https://doi.org/10.1038/s41589-021-00890-8

41 Duan, J. *et al.* GPCR activation and GRK2 assembly by a biased intracellular agonist. *Nature* **620**, 676–681 (2023). https://doi.org/10.1038/s41586-023-06395-9

42 Koehl, A. *et al.* Structure of the μ-opioid receptor–Gi protein complex. *Nature* **558**, 547–552 (2018). https://doi.org/10.1038/s41586-018-0219-7

43 Chen, Q. *et al.* Structures of rhodopsin in complex with G-protein-coupled receptor kinase 1. *Nature* **595**, 600–605 (2021). https://doi.org/10.1038/s41586-021-03721-x

44 Rasmussen, S. G. F. *et al.* Crystal Structure of the β2Adrenergic Receptor-Gs protein complex. *Nature* **477**, 549–555 (2011). https://doi.org/10.1038/nature10361

45 DeWire, S. M. & Violin, J. D. Biased ligands for better cardiovascular drugs: dissecting G-protein-coupled receptor pharmacology. *Circ Res* **109**, 205–216 (2011). https://doi.org/10.1161/circresaha.110.231308

46 Hilger, D., Masureel, M. & Kobilka, B. K. Structure and dynamics of GPCR signaling complexes. *Nat Struct Mol Biol* **25**, 4–12 (2018). https://doi.org/10.1038/s41594-017-0011-7

47 Oakley, R. H., Laporte, S. A., Holt, J. A., Caron, M. G. & Barak, L. S. Differential Affinities of Visual Arrestin, βArrestin1, and βArrestin2 for G Protein-coupled Receptors Delineate Two Major Classes of Receptors *. *Journal of Biological Chemistry* **275**, 17201–17210 (2000). https://doi.org/10.1074/jbc.M910348199

48 Kumari, P. *et al.* Core engagement with β-arrestin is dispensable for agonist-induced vasopressin receptor endocytosis and ERK activation. *Mol Biol Cell* **28**, 1003–1010 (2017). https://doi.org/10.1091/mbc.E16-12-0818

49 Cahill, T. J., 3rd *et al.* Distinct conformations of GPCR-β-arrestin complexes mediate desensitization, signaling, and endocytosis. *Proc Natl Acad Sci U S A* **114**, 2562–2567 (2017). https://doi.org/10.1073/pnas.1701529114

50 He, G. *et al.* A GPCR-G protein-β-arrestin megacomplex enabled by a versatile allosteric modulator. *Cell* (2026). https://doi.org/10.1016/j.cell.2025.12.023

51 Fleetwood, O., Matricon, P., Carlsson, J. & Delemotte, L. Energy Landscapes Reveal Agonist Control of G Protein-Coupled Receptor Activation via Microswitches. *Biochemistry* **59**, 880–891 (2020). https://doi.org/10.1021/acs.biochem.9b00842

52 Pettersen, E. F. *et al.* UCSF ChimeraX: Structure visualization for researchers, educators, and developers. *Protein Sci* **30**, 70–82 (2021). https://doi.org/10.1002/pro.3943

53 Emsley, P. & Cowtan, K. Coot: model-building tools for molecular graphics. *Acta Crystallogr D Biol Crystallogr* **60**, 2126–2132 (2004). https://doi.org/10.1107/s0907444904019158

54 Liebschner, D. *et al.* Macromolecular structure determination using X-rays, neutrons and electrons: recent developments in Phenix. *Acta Crystallogr D Struct Biol* **75**, 861–877 (2019). https://doi.org/10.1107/s2059798319011471

55 Williams, C. J. *et al.* MolProbity: More and better reference data for improved all-atom structure validation. *Protein Sci* **27**, 293–315 (2018). https://doi.org/10.1002/pro.3330

56 O'Boyle, N. M. *et al.* Open Babel: An open chemical toolbox. *J Cheminform* **3**, 33 (2011). https://doi.org/10.1186/1758-2946-3-33

57 Vanommeslaeghe, K. & MacKerell, A. D., Jr. Automation of the CHARMM General Force Field (CGenFF) I: bond perception and atom typing. *J Chem Inf Model* **52**, 3144–3154 (2012). https://doi.org/10.1021/ci300363c

58 Vanommeslaeghe, K., Raman, E. P. & MacKerell, A. D., Jr. Automation of the CHARMM General Force Field (CGenFF) II: assignment of bonded parameters and partial atomic charges. *J Chem Inf Model* **52**, 3155–3168 (2012). https://doi.org/10.1021/ci3003649

59 Humphrey, W., Dalke, A. & Schulten, K. VMD: visual molecular dynamics. *J Mol Graph* **14**, 33–38, 27–38 (1996). https://doi.org/10.1016/0263-7855(96)00018-5

60 Mayne, C. G., Saam, J., Schulten, K., Tajkhorshid, E. & Gumbart, J. C. Rapid parameterization of small molecules using the Force Field Toolkit. *J Comput Chem* **34**, 2757–2770 (2013). https://doi.org/10.1002/jcc.23422

61 Gaussian 16 Rev. C.01 (Wallingford, CT, 2016).

62 Zhang, L. & Hermans, J. Hydrophilicity of cavities in proteins. *Proteins* **24**, 433–438 (1996). https://doi.org/10.1002/(sici)1097-0134(199604)24:4<433::Aid-prot3>3.0.Co;2-f

63 Jo, S., Kim, T., Iyer, V. G. & Im, W. CHARMM-GUI: a web-based graphical user interface for CHARMM. *J Comput Chem* **29**, 1859–1865 (2008). https://doi.org/10.1002/jcc.20945

64 Brooks, B. R. *et al.* CHARMM: the biomolecular simulation program. *J Comput Chem* **30**, 1545–1614 (2009). https://doi.org/10.1002/jcc.21287

65 Lee, J. *et al.* CHARMM-GUI Input Generator for NAMD, GROMACS, AMBER, OpenMM, and CHARMM/OpenMM Simulations Using the CHARMM36 Additive Force Field. *J Chem Theory Comput* **12**, 405–413 (2016). https://doi.org/10.1021/acs.jctc.5b00935

66 Ballesteros, J. *et al.* Functional microdomains in G-protein-coupled receptors. The conserved arginine-cage motif in the gonadotropin-releasing hormone receptor. *J Biol Chem* **273**, 10445–10453 (1998). https://doi.org/10.1074/jbc.273.17.10445

67 Scheer, A., Fanelli, F., Costa, T., De Benedetti, P. G. & Cotecchia, S. The activation process of the alpha1B-adrenergic receptor: potential role of protonation and

hydrophobicity of a highly conserved aspartate. *Proc Natl Acad Sci U S A* **94**, 808–813 (1997). https://doi.org/10.1073/pnas.94.3.808

68 Jorgensen, W. L., Chandrasekhar, J., Madura, J. D., Impey, R. W. & Klein, M. L. Comparison of simple potential functions for simulating liquid water. *The Journal of Chemical Physics* **79**, 926–935 (1983). https://doi.org/10.1063/1.445869

69 Abraham, M. J. *et al.* GROMACS: High performance molecular simulations through multi-level parallelism from laptops to supercomputers. *SoftwareX* **1-2**, 19–25 (2015). https://doi.org/https://doi.org/10.1016/j.softx.2015.06.001

70 Hess, B., Bekker, H., Berendsen, H. J. C. & Fraaije, J. G. E. M. LINCS: A linear constraint solver for molecular simulations. *Journal of Computational Chemistry* **18**, 1463–1472 (1997). https://doi.org/https://doi.org/10.1002/(SICI)1096-987X(199709)18:12<1463::AID-JCC4>3.0.CO;2-H

71 Michaud-Agrawal, N., Denning, E. J., Woolf, T. B. & Beckstein, O. MDAnalysis: a toolkit for the analysis of molecular dynamics simulations. *J Comput Chem* **32**, 2319–2327 (2011). https://doi.org/10.1002/jcc.21787

72 Gowers, R. *et al.* MDAnalysis: A Python Package for the Rapid Analysis of Molecular Dynamics Simulations. *Proc. 15th Python Sci. Conf.*, 98–105 (2016). https://doi.org/10.25080/majora-629e541a-00e

73 McGibbon, R. T. *et al.* MDTraj: A Modern Open Library for the Analysis of Molecular Dynamics Trajectories. *Biophys J* **109**, 1528–1532 (2015). https://doi.org/10.1016/j.bpj.2015.08.015

74 Pérez-Hernández, G. & Hildebrand, P. W. mdciao: Accessible Analysis and Visualization of Molecular Dynamics Simulation Data. *PLoS Comput Biol* **21**, e1012837 (2025). https://doi.org/10.1371/journal.pcbi.1012837

75 Kandasamy, R. *et al.* Positive allosteric modulation of the mu-opioid receptor produces analgesia with reduced side effects. *Proceedings of the National Academy of Sciences* **118**, e2000017118 (2021). https://doi.org/doi:10.1073/pnas.2000017118

76 Kampfrath, M. *et al.* MDsrv: visual sharing and analysis of molecular dynamics simulations. *Nucleic Acids Res* **50**, W483–w489 (2022). https://doi.org/10.1093/nar/gkac398

Methods

Cells

HEK293T cells were obtained from the Cell Resource Center of Shanghai Institute for Biological Sciences (Chinese Academy of Sciences). *Spodoptera frugiperda* (Sf9) and *Trichoplusia ni* (Tni) insect cells were purchased from the Expression Systems (Cat# 94-001F and 94-002F). Expi293F cells were purchased from the Thermo Fisher (Cat# A14527)

Constructs

The cDNA of human wild type μ-opioid receptor (hMOR) was a gift from Prof. Jiahuai Han (Xiamen University). For protein purification, the sequence encoding for hMOR was cloned into a modified pFastBac1 vector with a haemagglutinin (HA) signal sequence at the N terminus. A

FLAG (DYKDDDDA) tag was inserted to the N terminus of hMOR to facilitate purification. For the structure determination of μOR-G_i bound to *(R)*-**141**, the sequence encoding for mouse μ-opioid receptor (μOR) was cloned into a modified pcDNA3.1 vector with a HA signal sequence and a FLAG tag at the N terminus. To facilitate the formation of μOR-G_i complex, the sequence encoding for miniG_i was fused to the C terminus of μOR. For cell-based β-arrestin recruitment assay, a SmBiT tag (VTGYRLFEEIL) was fused to the C terminus of hMOR after a flexible GS (GGSGGGGSGGSSSGG) linker. For cell-based GRK2 recruitment assay, a LgBiT tag (VTGYRLFEEIL) was fused to the C terminus of hMOR (1-383) after a flexible GS (GGSGGGGSGGSSSGG) linker[34]. All mutations were generated using the Quikchange strategy. All constructs were verified by DNA sequencing.

<u>High-throughput molecular docking and analog screen</u>

The high-resolution crystal structure of μOR-BU72 (PDB ID: 5C1M) was used for in-silico docking. The atomic model was first prepared in Maestro through the 'Protein Preparation Wizard' module, which included assigning bond orders, adding hydrogen atoms, modifying charges, and removing all crystal water molecules outside a 5 Å radius from the ligand. The entire system then was placed under the OPLS_2005 force field for energy minimization until convergence.

For ligand processing, compounds were prepared in Maestro's LigPrep, which including generating possible protonation states within a pH range of 7±2 using Epik, removing salt ions, generating tautomer, and producing all possible stereoisomers for chiral compounds with undetermined stereocenters. Each compound was allowed to produce up to 32 stereoisomers under the OPLS_2005 force field.

To determine the optimal binding site details and evaluate the screening parameters, we collected a validation set of ~300 structurally representative active compounds (K_i/K_D/IC_{50} < 1 μM) and 230 structurally representative inactive compounds. These were selected from a total of 4,000 compounds with known μOR activity by a k-means clustering analysis. Using this set, we confirmed that retaining waters 505 and 526 in the binding site improved docking performance.

Approximately 4.3 million commercially available compounds from BIONET, ChemBridge, ChemDiv, Enamine, InterBioScreen, Maybridge, Targetmol, and Vitas-M were used for screening. First, compounds were docked by Glide HTVS to eliminate molecules that cannot bind to the receptor, and the top 15% of poses were subsequently refined via GlideSP (standard precision). Poses with docking scores < −7 were subjected to a final round of Glide XP (extra precision)

782 docking. We then conducted a manual inspection of the poses with lower docking score, strain
783 energy and molecular weight. The selected compounds were then clustered to ensure the structural
784 diversity.
785 One billion on-demand synthesized compounds from Enamine were used for analog screen,
786 based on **64**'s ECFP-4 fingerprint and sub-structure (SMARTS: cNC(=O)NCC[N+]CcccO). Com-
787 pounds with a Tanimoto coefficient above 0.5 were selected for docking using the same Glide
788 protocol described above.
789
790 Protein expression and purification
791 The wild type hMOR was expressed and purified for the GTPase Glo assay. The wild type
792 hMOR was expressed in *Sf9* insect cells using Bac-to-Bac expression system. *Sf9* insect cells were
793 transfected at a density of 4×10^6 /ml with the baculoviruses of hMOR. After culturing for 48 hours,
794 the cells were harvested and stored at -80 °C. Frozen cells pellet were thawed and lysis in a buffer
795 containing 20 mM HEPES pH 7.5, 10 mM NaCl, 3 μM naloxone, 20% glycerol, 2 mg/ml iodoa-
796 cetamide and protease inhibitors. The membrane fraction was collected by centrifugation and then
797 solubilized with 20 mM HEPES pH 7.5, 300 mM NaCl, 1% (w/v) L-MNG (Anatrace), 0.3% CHS,
798 3 μM naloxone, 20% glycerol, 1 mg/ml iodoacetamide, 2 μl benzonase and protease inhibitor in
799 cold room for 1 hour. Supernatant was supplemented with 2 mM $CaCl_2$ and loaded into M1 Anti-
800 FLAG resin for purification. Receptor was finally eluted from resin in a buffer containing 20 mM
801 HEPES pH 7.5, 100 mM NaCl, 0.01% L-MNC, 0.001% CHS, 20% glycerol, 5 mM EDTA and
802 0.2 mg/ml FLAG peptide. The eluate was further purified by size exclusion chromatography (SEC)
803 on the Superdex 200 10/300 increase column (SD200, Cytiva). The monomeric fractions at ~ 12
804 ml retention volume were pooled, concentrated and flash froze for further use.
805 The heterotrimeric G_{i1} protein was expressed in *Tni* insect cells and purified as previously re-
806 ported. Briefly, *Tni* insect cells were transfected with a density of 3×10^6 /ml with the baculoviruses
807 including Gαi and Gβγ. After culturing for 48 hours, the cells were harvested and stored at -80 °C.
808 Frozen cells pellet were thawed and lysis in a buffer containing 20 mM HEPES pH 7.5, 5 mM
809 $MgCl_2$, 5 mM β-mercaptoethanol (β-ME), 10 μM GDP, 2 μl calf intestinal alkaline phosphatase
810 (CIP), 2 μl benzonase and protease inhibitors. The membrane fraction was collected by centrifu-
811 gation and then solubilized with 20 mM HEPES pH 7.5, 150 mM NaCl, 2 mM $MgCl_2$, 1% sodium
812 cholate, 0.05% DDM (Anatrace), 0.005% CHS, 5 mM β-ME, 10 μM GDP protease inhibitors and
813 20 mM imidazole in cold room for 1 hour. After centrifugation, the supernatant incubated with Ni-

NTA resin (Cytiva) for 2 hours in cold room. After incubation, the resin was washed in batch with 20 mM HEPES pH 7.5, 150 mM NaCl, 0.05% DDM, 0.005% CHS, 5 mM β-ME, 2 mM $MgCl_2$,10 μM GDP and 20 mM imidazole. Then the resin was transfer into a glass column and the detergent was slowly exchanged to 0.1% L-MNG and 0.01% CHS. The Gβγ protein was finally eluted with 20 mM HEPES pH 7.5, 100 mM NaCl, 0.1% L-MNG, 0.01% CHS, 2 mM $MgCl_2$,10 μM GDP, 300 mM imidazole and 100 μM TCEP. The eluted G_{i1} protein was treated with 5 μl λ protein phosphatase, 1 μl CIP, 1 μl Antarctic phosphatase. 3C protease was also added to cleave the His tag on Gβ protein. The protein was dialyzed in cold room overnight against the buffer containing 20 mM HEPES pH 7.5, 40 mM NaCl, 0.01% LMNG, 2 mM $MgCl_2$, 2 mM $MnCl_2$, 100 μM TCEP, 10 μM GDP and 5 mM imidazole. The second day, reverse Ni-NTA affinity chromatography was performed to remove uncleaved G_{i1} protein. The flow-through of Ni-NTA resin was loaded onto a MonoQ column and the G_{i1} protein was finally purified by anion exchange. The G_{i1} protein peak was collected, concentrated and flash froze for further use.

The mouse μOR-miniGi fusion protein was expressed and purified for structure determination. Plasmid encoding the μOR-miniGi was transfected into Expi293F cells with polyethylenimine (PEI) when the density is 2.5 $\times 10^6$ /ml. After culturing for 60 hours, the cells were harvested and stored at -80 °C. Frozen cells pellet were thawed and lysis in a buffer containing 20 mM HEPES pH 7.5, 10 mM NaCl, 50 μM *(R)*-**141**, 20% glycerol, 10 μM Tris (2- carboxyethyl) phosphine (TCEP) and protease inhibitors. The membrane fraction was collected by centrifugation and then solubilized with 20 mM HEPES pH 7.5, 500 mM NaCl, 1% L-MNG, 0.3% CHS, 0.3% CHAPS, 50 μM *(R)*-**141**, 20% glycerol, 2 mM $CaCl_2$, 10 μM TCEP, 2 μl benzonase and protease inhibitor in cold room for 2 hours. After centrifugation, the supernatant was loaded into M1 Anti-FLAG resin for purification. μOR-miniGi protein was eluted from the resin using the buffer containing 20 mM HEPES pH 7.5, 100 mM NaCl, 0.01% L-MNC, 0.001% CHS, 20% glycerol, 50 μM *(R)*-**141**, 5 mM EDTA, 10 μM TCEP and 0.2 mg/ml FLAG peptide. The eluate was further purified by SEC using a SD200 column using the buffer containing 20 mM HEPES pH 7.5, 100 mM NaCl, 0.01% LMNG, 0.001% CHS, 10 μM TCEP and 50 μM *(R)*-**141**. The fractions containing monomeric μOR-miniGi were collected and concentrated to form a complex with Gβγ and scFv16.

The Gβγ protein was expressed in *Tni* insect cells and purified as previously reported. Briefly, *Tni* insect cells were transfected a density of 3×10^6 /ml with a single bicistronic baculovirus encoding both the Gβ1 and Gγ2. After culturing for 48 hours, the cells were harvested and stored at -80 °C. Frozen cells pellet were thawed and lysis in a buffer containing 20 mM HEPES pH 7.5, 10

mM NaCl, 5 mM β-ME and protease inhibitors. The membrane fraction was collected by centrifugation and then solubilized with 20 mM HEPES pH 7.5, 150 mM NaCl, 1% sodium cholate, 0.05% DDM, 0.005% CHS, 5 mM β-ME, 2 μl benzonase, protease inhibitors and 20 mM imidazole in cold room for 1 hour. After centrifugation, the supernatant incubated with Ni-NTA resin for 2 hours in cold room. After incubation, the resin was washed in batch with 20 mM HEPES pH 7.5, 150 mM NaCl, 0.05% DDM, 0.005% CHS, 5 mM β-ME and 20 mM imidazole. Then the resin was transfer into a glass column and the detergent was slowly exchanged to 0.1% L-MNG and 0.01% CHS. The Gβγ protein was finally eluted with 20 mM HEPES pH 7.5, 100 mM NaCl, 0.1% L-MNG, 0.01% CHS, 300 mM imidazole and 100 μM TCEP. Eluted protein was pooled and 3C protease was added to cleave the His-tag on Gβ. The protein was dialyzed overnight in cold room against the buffer containing 20 mM HEPES pH 7.5, 100 mM NaCl, 0.01% L-MNG, 0.001% CHS, 100 μM TCEP and 15 mM imidazole. The second day, reverse Ni-NTA affinity chromatography was performed to remove uncleaved Gβγ heterodimer. The resulting Gβγ was concentrated and flash froze for further use.

scFv16 was expressed in *Tni* insect cells and purified as previously reported. Briefly, *Tni* insect cells were transfected a density of 3×10^6 /ml with baculovirus of scFv16. After culturing for 60 hours, the supernatant of cells was collected and supplemented with 5 mM $CaCl_2$ and 5 mM $MgCl_2$. After 1 hour incubation, the supernatant was loaded onto Ni-NTA resin and the scFv16 was eluted in 20 mM HEPES pH 7.5, 500 mM NaCl, and 300 mM imidazole. The eluate was incubated with 3C protease overnight to cleave the C-terminal His tag. After dialysis into the buffer consisting of 20mM HEPES pH 7.5 and 100 mM NaCl and 15 mM imidazole, scFv16 was further purified by reverse Ni-NTA. The flow-through was collected and further purified using a SD200 column. The scFv16 fractions were pooled, concentrated, and flash frozen for further use.

μOR-LgBiT and GRK2-HiBiT were co-expressed in *Tni* insect cells using Bac-to-Bac baculovirus expression system. After 60 hours, cell pellets were collected and lysed in lysis buffer containing 20 mM HEPES, pH 7.5, 150 mM NaCl, 15% glycerol, 5 mM $MgCl_2$, protease inhibitors, 100 μM TCEP, 50 μM *(R)*-**141** and 10 μM stauroporine. The suspension was incubated at room temperature for 30 minutes before centrifugation at 18, 000 rpm for 15 minutes. The membrane was then resuspended using solubilization buffer containing 20 mM HEPES, pH 7.5, 150 mM NaCl, 15% glycerol, 5 mM $MgCl_2$, 1% LMNG, 0.1% CHS, protease inhibitors, 100 μM TCEP, 50 μM *(R)*-**141**, 10 μM stauroporine and benzonase. The suspension was incubated at 4 ℃ for 2 hours before centrifugation at 18, 000 rpm for 40 minutes. The supernatant was then incubated with pre-

equilibrated Ni resin overnight at 4 °C. The second day, the Ni resin was washed with 20 column volumes Ni-washing buffer containing 20 mM HEPES, pH 7.5, 150 mM NaCl, 10% glycerol, 5 mM $MgCl_2$, 2 mM $CaCl_2$, 0.02% L-MNG, 0.002% CHS, 20 μM imidazole, 10 μM TCEP, 50 μM *(R)*-**141** and 10 μM stauroporine. Then protein was eluted from the Ni resin using Ni-washing buffer supplemented with 250 mM imidazole. The eluate was then loaded into pre-equilibrated M1 anti-FLAG resin slowly. The M1 anti-FLAG resin was washed using M1-washing buffer containing 20 mM HEPES, pH 7.5, 150 mM NaCl, 5% glycerol, 5 mM $MgCl_2$, 2 mM $CaCl_2$, 0.01% L-MNG, 0.001% CHS, 10 μM TCEP, 50 μM *(R)*-**141** and 10 μM stauroporine. Finally, the protein was eluted from M1 anti-FLAG resin using M1-elution buffer containing 20 mM HEPES, pH 7.5, 150 mM NaCl, 5 mM $MgCl_2$, 0.003% L-MNG, 0.0003% CHS, 10 μM TCEP, 50 μM *(R)*-**141**, 10 μM stauroporine and 0.2 mg/ml FLAG peptide. The μOR-GRK2 complex as then concentrated using an Amicon Ultra Centrifugal Filter (MWCO100 kDa) and further purified using a Superose 6 Increase 10/300 GL column (Cytiva) pre-equilibrated with 20 mM HEPES, pH 7.5, 150 mM NaCl, 5 mM $MgCl_2$, 0.003% L-MNG, 0.0003% CHS, 100 μM TCEP, 100 μM *(R)*-**141** and 20 μM stauroporine. The peak fractions containing μOR-GRK2 complex were collected and concentrated to 5 mg/ml for cryo-EM analysis.

Isotopic ligand competition binding assay

Human μOR were expressed in *Sf9* insect cells with Bac-to-Bac expression system. For insect cell membrane preparation, 50 mL cells were centrifuged and homogenized in 8 mL lysis buffer (20mM Tris, pH 7.5, 1 mM EDTA, with protease inhibitors). The lysate solution was centrifuged at 600 rpm for 10 min. The supernatant was then isolated and centrifuged at 18,000 rpm for 20 min. Finally, the membrane-containing pellet was resuspended with binding buffer (20 mM HEPES, pH 7.5, 100 mM NaCl).

For single point isotopic ligand competition binding assay, 100μL diluted membrane-suspension was incubated 100 μM cold compounds and ~ 2 nM [^{3}H]-DPN in a buffer containing 20 mM HEPES, pH 7.5, 100 mM NaCl and 0.5 mg/mL BSA, to a final volume of 500μL and incubated for 2 h with shaking at 220 rpm. To determine IC_{50} for these compounds, 100μL diluted membrane-suspension was incubated with varying concentration cold compounds and 2 nM [^{3}H]-DPN in a buffer containing 20 mM HEPES, pH 7.5, 100 mM NaCl and 0.5 mg/mL BSA, to a final volume of 500μL and incubated for 2 h with shaking at 220 rpm. After incubation, membranes were collected by filtration using Brandel 48-well harvester and filter papers containing the membrane

were incubated with 3 mL OptiPhase HiSafe 3 liquid scintillation cocktail overnight and the radioactivity was counted by Microbeta2 scintillation counter. The radioactivity was counted by Microbeta2 scintillation counter. Binding curves were fitted by GraphPad Prism 9.0 (GraphPad LLC, CA).

GTPase Glo assay

Purified hMOR and G_{i1} protein were diluted to 1 μM and mixed with 20 mM HEPES pH 7.5, 100 mM NaCl, 0.01% L-MNG, 0.001% CHS and 20 μM GTP in the presence of 10 μM various compounds, 10 μM DAMGO and naloxone were used as control (apo receptor was also set up as a control). The protein was incubated at room temperature with gentle sharking for 2 hours. After incubation, equal volume of GTPase-Glo reagent (Promega) containing 10 μM ADP was added to terminate the reaction. After 30 minutes, equal volume of detection reagent (Promega) was added and the luminescence of each group was measured using a multiplate reader.

Synthesis of *(R)*-**141** and *(S)*-**141**

For *(R)*-**141,** to obtain tert-Butyl (R)-(1-(3-(benzyloxy)benzyl)piperidin-3-yl)carbamate **(2)**, a stirred solution of *(R)*-3-Boc-aminopiperidine (1 g, 5 mmol, 1 eq) in DCM (20 mL) was prepared and treated with 3-(benzyloxy)benzaldehyde (2.12 g, 10 mmol, 2 eq) at room temperature (RT), followed by the addition of a few drops of acetic acid. The reaction mixture was stirred at RT for 1 hour before sodium cyanoborohydride (628 mg, 10 mmol, 2 eq) was added. Stirring was continued for an additional 12 hours. The reaction was then quenched with saturated $NaHCO_3$ solution (30 mL), and the resulting mixture was extracted with DCM (2 × 30 mL). The combined organic layers were washed with brine and dried over anhydrous Na_2SO_4. The crude product was purified by flash column chromatography, yielding compound **2** as a colorless oil (1.60 g, 81%). Then, a stirred solution of tert-butyl *(S)*-(1-(3-(benzyloxy) benzyl) piperidin-3-yl) carbamate (1.6 g, 4 mmol) in DCM (20 mL) was cooled to 0°C, and trifluoroacetic acid (4.5 mL, 60 mmol, 15 eq) was added dropwise. The reaction mixture was stirred at 0°C for 4 hours. Afterward, 4N NaOH solution was added to adjust the pH to neutral. The resulting mixture was extracted with DCM (3 × 30 mL), and the combined organic layers were washed with brine, dried over anhydrous Na_2SO_4, and concentrated under reduced pressure using a rotary evaporator. The reaction afforded compound **3** as a yellow oil (1.12 g, 93% yield). After that, 5-Ethyl-1H-pyrrole-2-carboxylic acid (211 mg, 1.52 mmol, 1 eq) and HOAt (248 mg, 3.04 mmol, 2 eq) were dissolved in DMF (8 mL) and stirred for

10 minutes. *(R)*-1-(3-(benzyloxy) benzyl) piperidin-3-amine (450 mg, 1.52 mmol, 1 eq) was then added, followed by NMM (118 μL, 1.06 mmol, 0.7 eq) at 0°C. After stirring for 5 minutes, EDCI (349 mg, 3.04 mmol, 2 eq) was introduced, and the reaction mixture was stirred at room temperature for 12 hours. The mixture was extracted with EtOAc (3 × 30 mL), and the combined organic layers were washed with brine, dried over anhydrous Na_2SO_4, and concentrated under reduced pressure. The crude product was purified by flash column chromatography, affording compound **4** as a yellow oil (380 mg, 60% yield). Finally, N-(1-(3-(Benzyloxy) benzyl) piperidin-3-yl)-5-ethyl-1H-pyrrole-2-carboxamide (100 mg, 0.24 mmol) was dissolved in MeOH (10 mL), and 10% palladium on carbon (38 mg) was added. The reaction mixture was subjected to a hydrogen atmosphere and stirred for 4 hours. After confirming the completion of the reaction, the catalyst was removed by filtration through diatomaceous earth, and the filter cake was washed thoroughly with MeOH. The combined filtrates were concentrated to dryness under reduced pressure. The residue was purified by silica gel column chromatography, affording *(R)*-**141** as a white solid (38 mg, 49% yield). *(S)*-**141** was synthesized through the same procedure used for *(R)*-**141** by replacing *(R)*-3-Boc-aminopiperidine with *(S)*-3-Boc-aminopiperidine (**1'**).

Cryo-EM sample preparation, image collection and data process

To prepare the complex of μOR-Gi-*(R)*-**141**, the concentrated μOR-miniGi-*(R)*-**141** was incubated with 1.2 molar excess Gβγ and scFv16 at room temperature for 1 hour. After incubation, the protein was concentrated and purified by SEC using a SD200 column in a buffer containing 20 mM HEPES pH 7.5, 100 mM NaCl, 0.002% LMNG, 0.0002% CHS, 100 μM TCEP and 50 μM *(R)*-**141**. The monomeric peak representing μOR-Gi-*(R)*-**141** complex was collected and concentrated for cryo-EM grids preparation.

To prepare the cryo-EM grids, 3.5 μl μOR-Gi-*(R)*-**141** or μOR-GRK2-*(R)*-**141** complex was loaded onto glow-discharged holey carbon grids (Quantifoil Au R1.2/1.3, 300 mesh). The grids were blotted for 4.5 seconds and flash-frozen in liquid ethane using a Vitrobot (Mark IV, Thermo Fisher Scientific). The data collection was conducted on a 300 kV Titan Krios (Shuimu Biosciences). The movies were captured with a bin2 pixel size of 1.08 Å using the super-resolution counting mode of SerialEM, with a defocus range of -1.1 to -1.6 μm. The total dose is about 50 e-/$Å^2$ for each stack. Movies were collected and subjected to beam-induced motion correcting by using MotionCor2 for further data process.

For μOR-Gi-*(R)*-**141** complex, a total of 1,887 micrographs were imported into cryoSPARC. Using a template picker (template generated from EMD-25613), 2,327,296 particles were selected. Following iterative 2D classification, 700,133 particles exhibiting clear features of the GPCR-G protein complex were selected and re-extracted with a box size of 256 pixels. These particles underwent *ab* initio reconstruction, heterogeneous refinement, non-uniform refinement, and local refinement. A local mask focused on the receptor region was applied during iterative 3D classification to enhance ligand density. Ultimately, 59,327 particles were used to reconstruct the final map, achieving an overall resolution of 3.08 Å. The local resolution was estimated in cryoSPARC using default parameters

For μOR-GRK2-*(R)*-**141** complex, 8,783 micrographs were imported into cryoSPARC. Using a template picker (template generated from EMD-36474), 12,471,403 particles were selected and extracted for iterative 2D classification and *ab* initio reconstruction. Among the four maps generated by *ab* initio reconstruction, one exhibited clear feature of the GPCR-GRK2 complex. Subsequently, an additional batch of 5,178 micrographs was imported into cryoSPARC, yielding a total of 13,530,183 particles for heterogeneous refinement using the previously generated *ab* initio map. Following this, 2,173,916 particles were selected and re-extracted with a box size of 256 pixels. 2D classification was then employed to remove obvious junk particles prior to heterogeneous refinement. After classification, 418,929 particles were retained and subjected to *ab* initio reconstruction. Of these, 277,529 particles were reconstructed into a map with clear features. These particles underwent further non-uniform refinement and focused local refinement, ultimately yielding an overall resolution of 3.08 Å. The local resolution was estimated in cryoSPARC using default parameters

Model building and refinement

For the μOR-Gi-*(R)*-**141** complex, the model of μOR-Gi-scFv16-DAMGO (PDB ID: 6DDE) was first docked into the refined cryo-EM map using UCSF ChimeraX[52], followed by iterative manual adjustments in Coot 0.9.3[53]. For the μOR-GRK2-*(R)*-**141** complex, the receptor part was modeled using μOR-Gi-scFv16-TRV130 (PDB ID: 8EFB), while the GRK2 part was based on NTSR-GRK2-Gαq (PDB ID: 8JPB). These models were first docked into the refined cryo-EM map in UCSF ChimeraX, followed by iterative manual adjustments in Coot 0.9.3. Models and restraints for *(R)*-**141** and staurosporine were generated using eLBOW in Phenix, and the final complex models were refined via Phenix Real Space Refinement[54]. The structural models were

analyzed in UCSF ChimeraX. The final refinement statistics, as shown in Extended Data Table.1, were validated using the "Comprehensive validation (cryo-EM)" module in Phenix[55]. All related figures were prepared in UCSF ChimeraX.

NanoBiT G protein dissociation assay

HEK293T cells were seeded in 6-well dishes at a density of 2 × 10^5 cells per ml DMEM supplemented with 10% FBS, penicillin and streptomycin 1 day before transfection. For each well, transfection solution is prepared by combining 500 ul Opti-MEM, 25 ul 1 mg/ml PEI and a plasmid mixture containing 2 μg hMOR, 400 ng LgBiT-Gα_{i1} (or other subtype if Gαi/o/z protein), 1 μg Gβ1 and 1 μg SmBiT-Gγ2(C68S). After 1 day, cells are treated with 0.05% Trypsin and collected with HBSS containing 20 mM HEPES pH 7.5 and 10 μM coelenterazine. Cells are dispensed into 96-well plate at a volume of 90 μl per well. After 1-hour incubation at room temperature, the plate was measured for baseline luminescence. Then 10 ul of varying concentration of ligands was manually added to each well and luminescence was counted for 10 min with an interval of 60 sec. Does-response curves were fitted by GraphPad Prism 9.0 (GraphPad LLC, CA).

NanoBiT GRK engagement and β-arrestin recruitment assay

HEK293T cells were seeded in 6-well dishes at a density of 2 × 10^5 cells per ml DMEM supplemented with 10% FBS, penicillin and streptomycin 1 day before transfection. For each well, transfection solution is prepared by combining 500 ul Opti-MEM, 25 ul 1 mg/ml PEI and a plasmid mixture containing 1 μg hMOR-LgBiT and 3 μg SmBiT-GRK2 (a gift from Prof. Eric H. Xu) or 2 μg hMOR-smBiT, 2 μg GRK2 and 200 ng LgBiT-β-arrestinEE (for β-arrestin recruitment). After 1 day, cells are treated with 0.05% Trypsin and collected with HBSS containing 20 mM HEPES pH=7.5 and 10 μM coelenterazine. Cells are dispensed into 96-well plate at a volume of 90 μl per well. After 2-hour incubation at RT, the plate was measured for baseline luminescence. Then 10 ul of varying concentration of ligands was manually added to each well and luminescence was counted for 10 min with an interval of 60 sec. Does-response curves were fitted by GraphPad Prism 9.0 (GraphPad LLC, CA).

Generation of Ligand Parameters for Molecular Dynamics Simulation

DAMGO and *(R)*-**141** were prepared and parameterized for molecular dynamics simulations using the *CHARMM* additive force field and the *CHARMM General Force Field* (*CGenFF*). First,

initial 3D structures were generated and missing hydrogen atoms were added assuming physiological conditions (pH 7.0). Protonation states were assigned based on predicted *p*Ka values, and reasonable tautomers were selected. Structure preparation and hydrogen addition were performed using *Open Babel*[56].

Initial atom types, bonded parameters, and partial atomic charges were assigned by analogy using the *CGenFF* program through the *ParamChem* web server[57,58].This step generates *CHARMM* compatible topology and parameter files and provides penalty scores that indicate the reliability of each assigned parameter.

These penalty scores were used to evaluate parameter quality, with values below 10 considered acceptable and those between 10 and 50 inspected more carefully. Parameters with penalties above 50 were considered unreliable and therefore reparametrized. The parametrization of DAMGO was within the acceptable margins, while for *(R)*-**141**, several parameters, mainly partial charges, exceeded this threshold and were selected for refinement[57,58].

Reparameterization was performed using the Force Field Toolkit (ffTK) implemented in *VMD*[59,60]. Quantum mechanical reference calculations were carried out with Gaussian 16[61]. Geometry optimizations and vibrational frequency calculations were performed at the MP2/6-31G* level of theory to obtain target bond lengths and angles, following standard *CHARMM* parameterization procedures[57,60].

Partial atomic charges were optimized based on electrostatic potential (ESP) calculations at the HF/6-31G* level, in line with the *CHARMM* force field philosophy[57,58]. The final parameter sets for *(R)*-**141** were obtained after several iterations, until good agreement between molecular mechanics and quantum mechanical reference data was achieved.

Molecular dynamics simulation and analysis

A total of four different μOR-ligand configurations were prepared for molecular dynamics (MD) simulations. The simulations of *(R)*-**141** bound to μOR were based on the cryo-EM structure of the *(R)*-**141** bound μOR-Gi-protein complex reported in this manuscript. DAMGO bound μOR simulations were based on a published DAMGO-μOR-Gi protein complex (PDB:8K9K). The μOR constructs were well resolved except for the N-terminus (M1–S66) and a C-terminal tail (E351–P400); three additional residues (F352$^{8.57}$–I354$^{8.59}$) were added to the μOR construct's C-

terminal end to preserve the palmitoylation site at C353$^{8.58}$. The resolved N-terminal and C-terminal ends of the μOR structure were capped with neutral groups (N-terminal: acetylated; C-terminal: methylated) to avoid spurious interactions.

The μOR simulation setups consisted of ligand-bound μOR lacking any intracellular transducer, either bound to DAMGO or to the novel *(R)*-**141** ligand. In both cases the G-protein was removed to increase receptor flexibility. Two single-point mutant structures were from the wild-type templates: N$^{7.45}$Q in the *(R)*-**141**-bound system and Y$^{7.55}$F in the DAMGO-bound system utilizing *PyMOL* (version 2.5.2, Schrödinger, LLC).

All μOR systems were processed with DOWSER[62]to fill internal cavities. The prepared μOR systems were setup for MD simulation using the *CHARMM-GUI* web service[63-65]. The simulation parameters for the ligands were needed to be created and details of the ligand parametrization are provided in the section below.

Within the CHARMM-GUI simulation setup aspartate residues D116$^{2.50}$ and D166$^{3.49}$ of μOR were protonated, reflecting a characteristic feature of active class-A GPCRs[66,67]. A disulfide bridge was introduced between Cys142$^{3.25}$ and Cys219$^{45.50}$. Furthermore, Cys353$^{8.58}$ was palmitoylated, due to it being an important membrane-anchoring modification[67].

The prepared structures were embedded in a POPC bilayer and subsequently solvated with TIP3 water within a cubic simulation box[68]. Ions (Na^+/Cl^-) were added to achieve a physiological 0.15 M, neutral salt concentration. The number of atoms, lipid molecules, waters, and box dimensions for each of the five setups are summarized in:

Setup	Sim. Box (Å^3)	Num. POPC: (Upper leaflet, lower leaflet)	Num. TIP3	Num. Na+, Num. Cl-	Total atom number
μOR_WT_*(R)*-**141**	90x90x103	101, 103	15110	39, 55	77467
μOR_WT_DAMGO	90x90x108	100, 101	16257	42, 58	80680
μOR_N$^{7.45}$Q_*(R)*-**141**	90x90x103	101, 103	15132	39, 55	77536
μOR_Y$^{7.53}$F_DAMGO	90x90x108	100, 101	16322	42, 58	81008

The finalized systems were simulated at 310.15 K under a pressure of 1.013 bar using an NPT ensemble in *GROMACS 2024.2* with the *CHARMM36* force field (optimized WYF parameters)[69,70]. A 2-fs time step was employed together with the LINCS algorithm[70]. Energy minimization was carried out with the steepest-descent method, using a convergence threshold of 1000 $kJ \cdot mol^{-1} \cdot nm^{-1}$. Equilibration proceeded through six successive stages in which restraints on protein side-chains, the protein backbone, and the 1-palmitoyl-2-oleoyl-sn-glycero-3-phosphocholine (POPC) lipids were gradually released.

For the μOR systems that lacked an intracellular transducer, a cumulative simulation time of 15 × 3.5 μs was accumulated per system. Individual simulation runs were independently started by producing randomized starting velocities. Trajectory analysis was performed with custom Python scripts that employed the *MDAnalysis*[71,72], *MDTraj*[73], *mdciao*[74] and *mdxplain* (https://github.com/mdx-toolbox/mdxplain) libraries. Structural images were rendered with VMD[59] and ChimeraX[52].

Receptor cell surface expression level

HEK293T cells were seeded in 24-well dishes at a density of 2×10^5 cells per ml DMEM supplemented with 10% FBS, penicillin and streptomycin 1 day before transfection. For each well, transfection solution is prepared by combining 125 ul Opti-MEM, 6 ul 1 mg/ml PEI and 1 μg HA-FLAG-hMOR or empty pcDNA3.1 (vehicle). After 1 day, cells are treated with 0.05% Trypsin and collected with HBSS containing 20 mM HEPES pH=7.5 to a volume is 200 ul, 10 nM AlexaFlour-488 labelled M1-anti FLAG antibody are mixed with cells for 15 min in dark. After incubation, cells are washed with HBSS containing 20 mM HEPES pH=7.5 for twice. Cell surface fluorescence is determined by Flow Cytometer at 488 wavelengths. Data are processed in FlowJo to calculate Mean FITC intensity.

In virto phosphorylation assay of μOR

The μOR for phosphorylation detection was purified following a similar protocol as previously described, with different phosphatases (alkaline phosphatase, lambda phosphatase, and Antarctic phosphatase; New England Biolabs) added during the solubilization step. The purified μOR was diluted in phosphorylation buffer (20 mM Tris-HCl, pH 7.5, 30 mM NaCl, 5 mM $MgCl_2$, 2 mM $NaVO_3$, 1 mM ATP, 40 μM C8-PIP_2, 50 μM TCEP, 0.001% MNG, and 0.0001% CHS) to a final receptor concentration of 4 μM. The diluted receptors were then supplemented with either buffer

(apo state), 40 μM *(R)*-**141**, or 40 μM DAMGO. GRK2 was added to the reaction mixture to a final concentration of 200 nM. After incubation at 30°C for 60 minutes, phosphorylation was terminated by adding 50 mM EDTA. The phosphorylation levels and specific sites on μOR were detected using mass spectrometry, with a μOR-only sample (without GRK2) serving as the negative control.

After SDS-PAGE, gel bands of proteins were excised for in-gel digestion, Briefly, proteins were disulfide reduced with 5 mM dithiothreitol (DTT) and alkylated with 11 mM iodoacetamide. In-gel digestion was performed using sequencing grade-modified chymotrypsin in 50 mM ammonium bicarbonate at 25 °C overnight. The peptides were extracted twice with 1% trifluoroacetic acid in 50% acetonitrile aqueous solution for 30 min. The peptide extracts were then centrifuged in a SpeedVac to reduce the volume. For LC-MS/MS analysis, the peptides were separated by a 120 min gradient elution at a flow rate 0.300 μl/min with a Ascend HPLC system. The analytical column was a home-made fused silica capillary column (100 μm ID, 400 mm length; Upchurch, Oak Harbor, WA) packed with C-18 resin (300 Å, 5 μm, Varian, Lexington, MA). Mobile phase 9 A consisted of 0.1% formic acid, and mobile phase B consisted of 100% acetonitrile and 0.1% formic acid. The Ascend mass spectrometer was operated in the data-dependent acquisition mode using Xcalibur 2.1.2 software (Thermo-Fisher Scientific, USA) and there was a single full-scan mass spectrum in the orbitrap (350-1600 m/z, 120,000 resolution) followed by 10 data-dependent MS/MS scans at collision energy (HCD).The LC-MS/MS spectra from each run were searched against sequence of human μOR using a commercial software of Proteome Discoverer (Version PD2.3, Thermo-Fisher Scientific, USA).

Pharmacokinetics of *(R)*-**141**

Adult male ICR (aged 6-8 weeks) were used to determine the blood-brain barrier penetration ability of *(R)*-**141**. Mice were overnight fasting before dosing. *(R)*-**141**was dissolved in a buffer containing 5% DMSO + 10% Solutol HS 15 + 85% Saline, and was administrated intravenously or orally. Each time point after injection, blood samples were collected from isoflurane-anesthetized mice into EDTA-K2 anticoagulant-containing tubes, the samples were then centrifuged for 30 minutes to obtain the plasma. Whole blood samples were kept on wet ice before centrifugation. After blood sampling, euthanized animals via CO_2 inhalation and collected brain tissue samples. All brain tissue samples were rinsed with saline, wiped dry with filter paper, and weighed after surface moisture removal. A total of 30 plasma and 30 brain tissue samples are collected. All collected plasma and brain tissue samples are stored on dry ice or frozen until analysis.

For analysis, determine the concentrations of the test compound in 6 mouse plasma samples and 6 brain tissue samples by LC-MS/MS. Prepare the calibration curves using blank plasma for quantifying plasma samples and blank brain homogenate for quantifying all brain tissue samples. Ensure that at least one set of calibration curves and QC samples are prepared for each blank matrix, with at least 3/4 of the standard curve samples having accuracy within ± 20% of their true concentrations (± 25% for LLOQ).

Formalin injection assay

Male C57BL/6J mice aged 8-10 weeks, sourced from Shanghai Shengchang Biotechnology Co., Ltd (Shanghai, China), were used for all in vivo experiments. The mice were housed in groups of 5 per cage under standardized conditions, with a temperature maintained at 23 ± 1℃, relative humidity of 60 ± 10 %, and a 12-hour light-dark cycle. Food and water were provided *ad libitum*. All experimental procedures were approved by the Institutional Animal Care and Use Committees (IACUC) of Shanghai Institute of Materia Medica, CAS (Approval No. 2024-02-GZB-17), and conducted in strict accordance with the guidelines for the Care and Use of Laboratory Animals.

(R)-**141** was prepared in a solution consisting of 5% dimethyl sulfoxide, 10% Solute-HS15, and 85% normal saline, and administered intraperitoneally (i.p.) at doses of 1, 2.5, 5 or 10 mg/kg. Morphine (morphine hydrochloride injection, 10 mg/ml, NORTHEAST PHARM in China) was diluted with 0.9% saline for i.p. injection at 5 and 10 mg/kg. The solvent formulation and route of administration for vehicle groups were identical to those used for *(R)*-**141**. A 4% Formalin solution (25 µl, Sigma-Aldrich) was injected subcutaneously into the plantar region of the right hind paw of the mouse. the formalin-induced nociception test was employed to evaluate the analgesic effects of *(R)*-**141**.The experiment was conducted using four transparent observation chambers (20 cm in diameter and 30 cm in height) placed on a transparent platform. 30 minutes before formalin test, mice were i.p. administered *(R)*-**141**, morphine, or vehicle, respectively, and then allowed to acclimate in the test chambers until the formalin injection. After the formalin injection, nociceptive behaviors (such as licking, shaking, and lifting of the injected paw) were recorded via video over a 60-minute observation period. The observation period was divided into two distinct phases: Phase 1 (0–10 minutes), representing the acute nociceptive response, and Phase 2 (10–60 minutes), reflecting the inflammatory pain response. The total duration of nociceptive behaviors during each phase was quantified and analyzed to assess the analgesic efficacy of the treatments.

Mouse whole-body plethysmography

Respiratory data from conscious, unrestrained mice were obtained using a whole-body plethysmography system (WBP-4M, Tow-Int Tech Co., Ltd., Shanghai, China), as previously described[30]. Before testing, mice were acclimated to the plethysmography device, which was equipped with four testing chambers and Buxco airflow transducers, for 30 minutes daily over two consecutive days. On the test day, mice were re-acclimated to the device, and baseline respiratory data were recorded for 10 minutes to ensure stability. After i.p. injection of *(R)*-**141**, morphine, or vehicle, respiratory data were continuously monitored and recorded for an additional 90 minutes. Key parameters, such as respiratory frequency (breaths per minute) and tidal volume, were analyzed and calculated using the integrated recording software.

Accumulated fecal boli quantification

The conspiratory effects of *(R)*-**141** and morphine were evaluated by measuring accumulated fecal boli, as previously described[75]. Mice were administered *(R)*-**141**, morphine, or vehicle via i.p. injection and promptly placed in brown plexiglass chambers equipped with mesh flooring. Fecal boli were collected from beneath the mesh, and the total count was recorded hourly for six hours.

Statistical analysis

Quantification methods and tools used are described in each relevant section of the methods or figure legends. The non-linear curve fit was performed using a three-parameter logistic equation [log (agonist vs response)] in GraphPad Prism and was shown as Mean ± SEM with at least 3 independent replicates.

For in vivo studies, statistical analyses and graphing were performed using GraphPad Prism software (version 8.0.2). Data were analyzed by one-way or two-way repeated-measures ANOVA (mixed-effects analysis), followed by Dunnett's post hoc tests. All data are expressed as means ± SEM, with statistical significance set at $P < 0.05$.

Data availability:

All data are presented in the main text or supplementary materials of the manuscript. For protein structures, the atomic coordinate for μOR-Gi-*(R)*-**141** and μOR-GRK2-*(R)*-**141** complexes have been deposited in the Protein Data Bank with the accession codes 24EU and 24EV, the EM map for μOR-G_i-*(R)*-**141** and μOR-GRK2-*(R)*-**141** complexes have been deposited in EMDB with the accession codes EMD-69465 and EMD-

69466. Fully atomistic MD trajectories are available online for direct and interactive 3D visualization in web browser as mdsrv[76] sessions here: μOR_wt-*(R)*-**141**: https://proteinformatics.uni-leipzig.de/mdsrv.html?load=file://_u-opioid/muOR_WT_141.js, μOR_$N^{7.45}$Q-*(R)*-**141**: https://proteinformatics.uni-leipzig.de/mdsrv.html?load=file://_u-opioid/muOR_MUT_141.js, μOR_wt-DAMGO: https://proteinformatics.uni-leipzig.de/mdsrv.html?load=file://_u-opioid/muOR_WT_DAMGO.js, μOR_$Y^{7.53}$F-DAMGO:https://proteinformatics.uni-leipzig.de/mdsrv.html?load=file://_u-opioid/muOR_MUT_DAMGO.js.

Acknowledgments: We thank Prof. Brian K. Kobilka for discussion and suggestions, Prof. Asuka Inoue for providing the plasmids for the NanoBiT assay and Prof. Eric H. Xu for providing the plasmid of HiBiT-GRK2 and SmBiT-GRK2. We also thank supports from the Tsinghua University Branch of China National Center for Protein Sciences (Beijing) as well as Shuimu Biosciences for supports with cryo-EM data collection. We would like to thank the high-performance computing (HPC) Service of FUB-IT, Freie Universität Berlin, for computing time. We gratefully acknowledge the scientific support and HPC resources provided by the Erlangen National High-Performance Computing Center (NHR@FAU) of the Friedrich-Alexander-Universität Erlangen-Nürnberg (FAU) under the NHR project p101ae NHR funding is provided by federal and Bavarian state authorities. NHR@FAU hardware is partially funded by the German Research Foundation (DFG) - 440719683. This work is supported by Tsinghua-Peking Center for Life Sciences (C.Y. and X.L.), Beijing Frontier Research Center for Biological Structure, Tsinghua University (G.H., C.Y., and X.L.), Strategic Priority Research Program of the Chinese Academy of Sciences (Grant ID: XDB0830403 to Z.G.), National Natural Science Foundation of China (Grant 32122041 to X.L.), Deutsche Forschungsgemeinschaft (DFG) through CRC 1423, project number 421152132 (C01 and Z04 to P.W.H.) and Tsinghua University Initiative Scientific Research Program (C.Y. and X.L.)

Author contributions:

Conceptualization: G.H. and X.L.. Methodology: G.H., M.P., H.X. and H.L.. Investigation: G.H., M.P., G.Y., H.L., H.X., M.S., H.B., X.G., S.Z, F.K., L.Z., X.S., and Q.M.. Visualization: G.H. M.P., H.L. and H.X.. Funding acquisition: C.Y., P.W.H. and X.L.. Project administration: G.H. and X.L.. Supervision: X.C., L.H., S.D., C.Y., Z.G., P.W.H. and X.L.. Writing – original draft: G.H. M.P., P.W.H. and X.L.. Writing – review & editing: G.H., M.P., H.X., H.L., H.B., P.W.H. and X.L..

Competing interests: Authors declare that they have no competing interests.

Correspondence and requests for materials should be addressed to Guodong He, Zhaobing Gao, Peter W. Hildebrand or Xiangyu Liu.

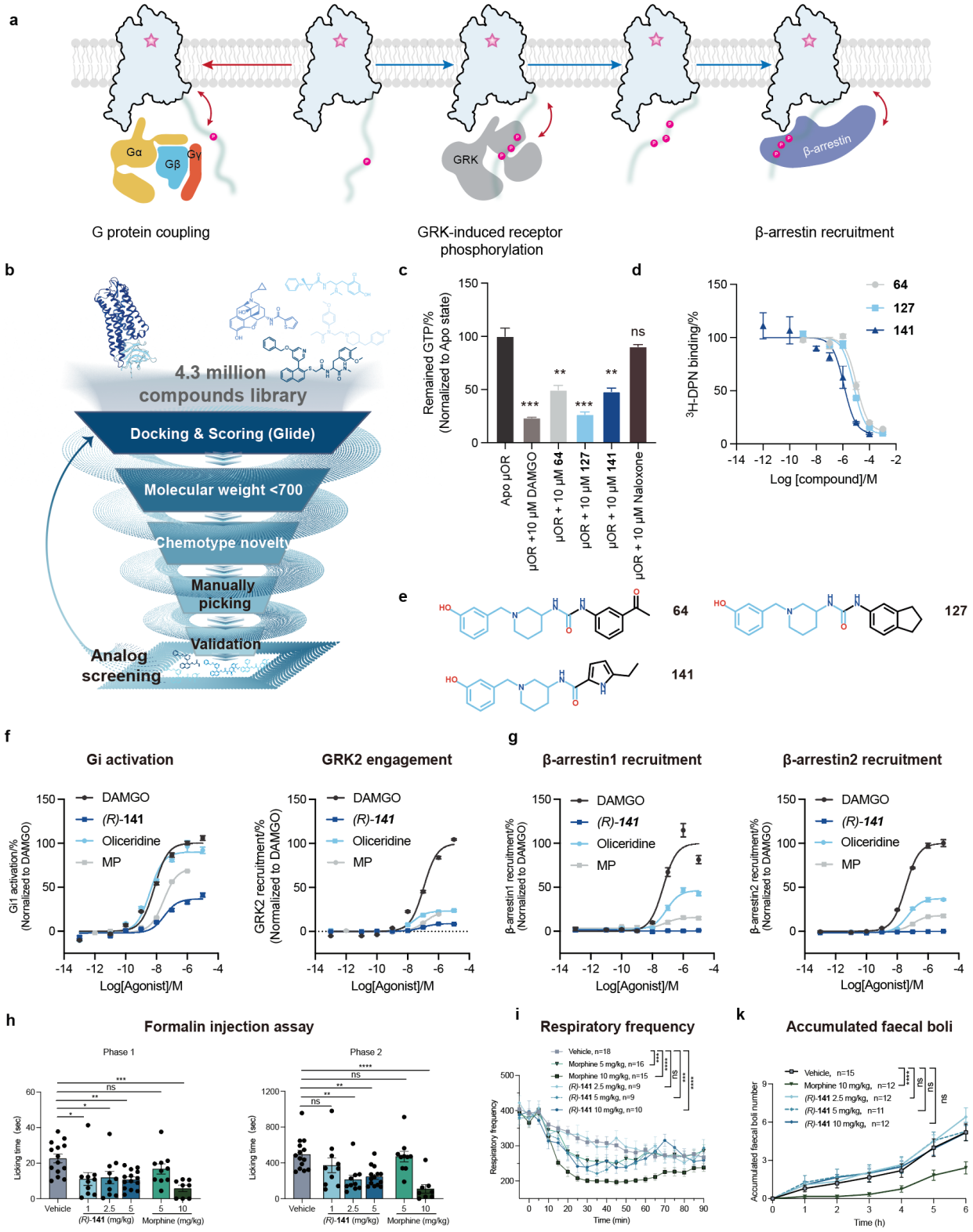

Fig. 1 | *(R)*-141 is a pronounced G protein-biased agonist of μOR with therapeutic potential. **a,** Complex triad of G protein, GRK and β-arrestin in GPCR signaling transition. **b**, The flowchart of high-throughput virtual screening. **c**, The agonistic function of **141** was verified by *in vitro*

GTPase-Glo assay. At 10 μM, **141** significantly accelerates the GTP turnover rate of Gi. Statistical significance was determined by unpaired *t*-test. ns $P > 0.05$, *$P < 0.05$, **$P < 0.01$. **d,** The affinity of **141** for μOR was determined by isotopic ligand competition assay; **141** exhibits an improved IC_{50} compared to **64** and **127**. **e,** The chemical scaffolds of compounds **64**, **127**, and **141**; they share an identical sub scaffold (colored in blue). **f-g,** The signaling profile of *(R)*-**141** indicates that it acts as a pronounced G protein-biased agonist of μOR, with minimal GRK2 engagement (**f**) and undetectable β-arrestin recruitment (**g**). The β-arrestin recruitment abilities of different agonists were evaluated in the presence of overexpressed GRK2. **h,** The analgesic effects of *(R)*-**141** were evaluated using a formalin injection assay, with morphine used as the positive control. Compared to vehicle, a low dose (2.5 mpk) of *(R)*-**141** exhibits significant analgesic effects, as reflected by reduced licking time, whereas 5 mpk morphine does not produce analgesic effects. **i,** Whole-body mouse plethysmography shows that an equi-analgesic dose of *(R)*-**141** (2.5 mpk) has no effect on respiration versus vehicle. Although higher doses of *(R)*-**141** exhibit some respiratory depression, the influence recovers rapidly. In contrast, 5 mpk morphine (a sub-analgesic dose) induces respiratory depression 10 minutes after administration. **j,** The conspiratory effects of *(R)*-**141** and morphine compared to vehicle assessed by accumulated faecal boli.

Data are shown as mean ± S.E.M. of at least three independent replicates for panels **c,d,f** and **g**. Data are shown as mean ± S.E.M with n>8 for panels **h-j**. Statistical significance was determined by one-way or two-way repeated-measures ANOVA (mixed-effects analysis), followed by Dunnett's post hoc tests. ns $P > 0.05$, *$P < 0.05$, **$P < 0.01$, ***$P < 0.001$, ****$P < 0.0001$.

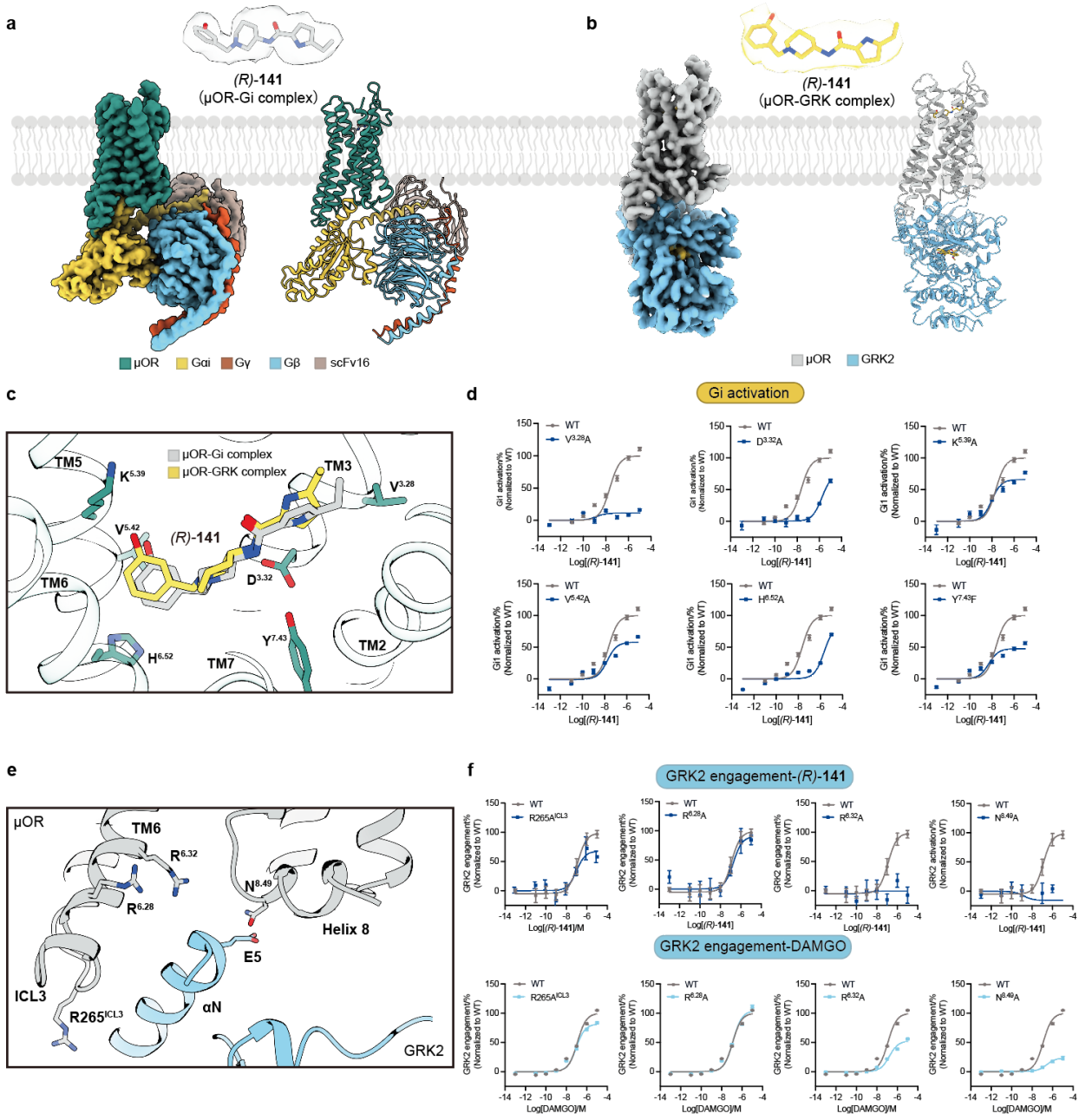

Fig. 2 | Cryo-EM structures of μOR-Gi-*(R)*-141 and μOR-GRK2-*(R)*-141. a, Cryo-EM density map and atomic model of the μOR-Gi-*(R)*-**141** complex. **b,** Cryo-EM density map and atomic model of the μOR-GRK2-*(R)*-**141** complex. **c,** *(R)*-**141** binds to the orthosteric pocket of μOR in both structures, adopting similar conformation. **d,** Mutations of representative residues within the ligand-binding pocket were performed to validate the binding mode of *(R)*-**141** observed in the cryo-EM structures. The functional impact of these mutations was evaluated by monitoring G protein activation levels upon *(R)*-**141** stimulation. **e,** Structure of μOR-GRK2 interface, the αN helix

of GRK2 inserts into the intracellular pocket of μOR. **f,** Mutagenesis studies for residues at the interface of μOR-GRK2.

Data are shown as mean ± S.E.M. of at least three independent replicates for panels **d** and **f**. The expression levels of each mutant are represented in Extended Data Figure. 3j.

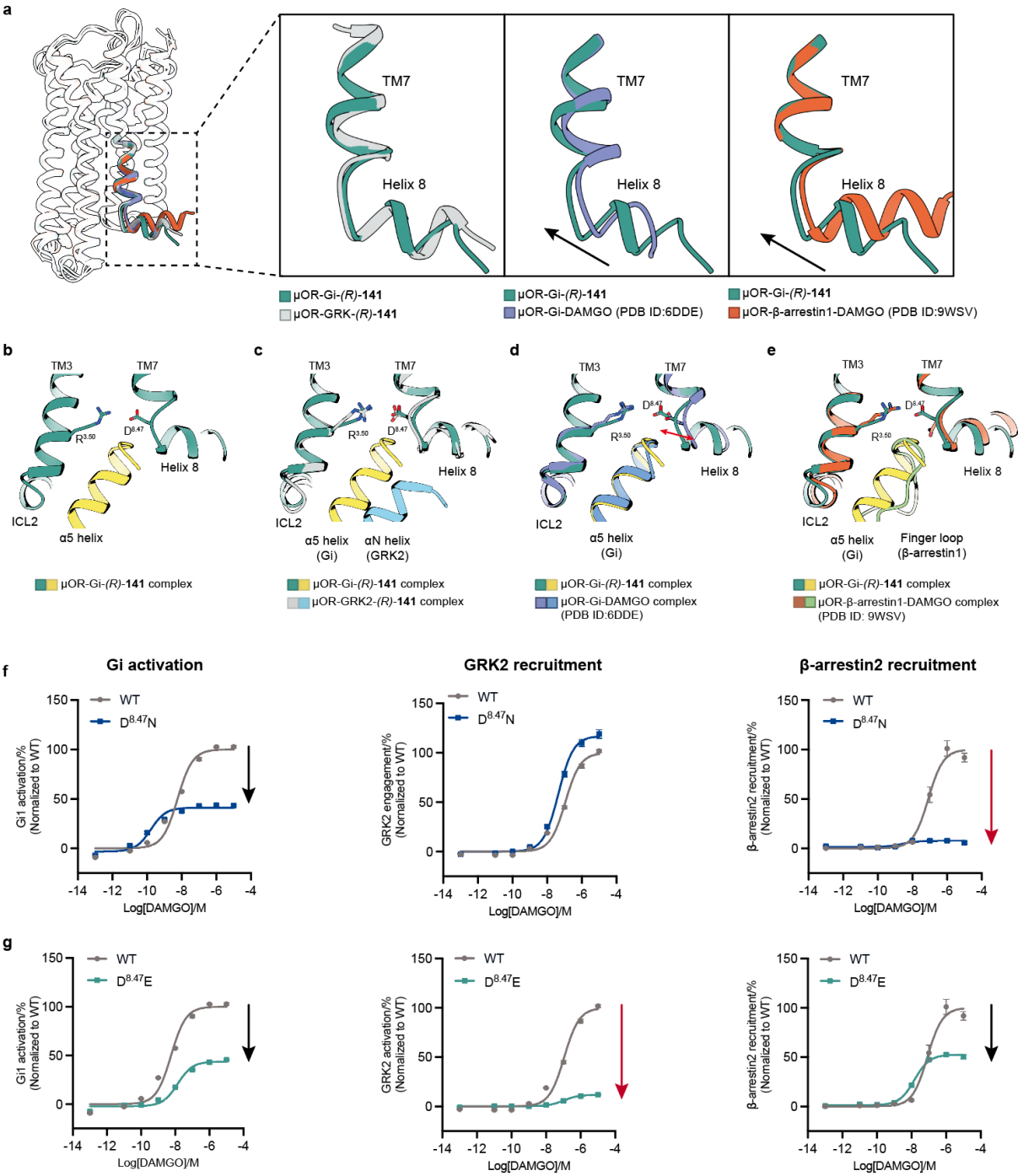

Fig. 3 | R-D ionic lock and transducer decoupling. a, Structural comparison of μOR in different signaling complexes. Structural alignment of μOR-Gi-*(R)*-**141**, μOR-GRK2-*(R)*-**141**, μOR-Gi-DAMGO (PDB ID: 6DDE), and μOR-β-arrestin-DAMGO (PDB ID: 9WSV). While the majority of the μOR maintains a conserved overall conformation, distinct structural divergences are observed in the TM7 and Helix 8 regions. *(R)*-**141** stabilizes an inward movement of TM7 and Helix

8. **b-c,** An ionic lock between $R^{3.50}$ and $D^{8.47}$ is observed in both μOR-Gi-*(R)*-**141** (**b**) and μOR-GRK2-*(R)*-**141** (**c**) structures. **d-e,** The $R^{3.50}$-$D^{8.47}$ ionic lock is absent in both the μOR-Gi-DAMGO (PDB ID: 6DDE, **d**) and μOR-β-arrestin-DAMGO (PDB ID: 9WSV, **e**) structures, owing to insufficient proximity or unfavorable side-chain orientations. **f-g,** Mutagenesis studies suggest a decoupling of GRK2 engagement from β-arrestin recruitment. Both $D^{8.47}$N and $D^{8.47}$E mutants maintain comparable G protein signaling. However, while $D^{8.47}$N retains the ability to engage GRK2, its β-arrestin recruitment is significantly diminished (**f**). In contrast, the $D^{8.47}$E mutant maintains effective β-arrestin recruitment despite minimal GRK2 engagement (**g**).

Data are shown as mean ± S.E.M. of at least three independent replicates for panels **f-g**. The expression levels of each mutant are represented in Extend Data Fig.3J.

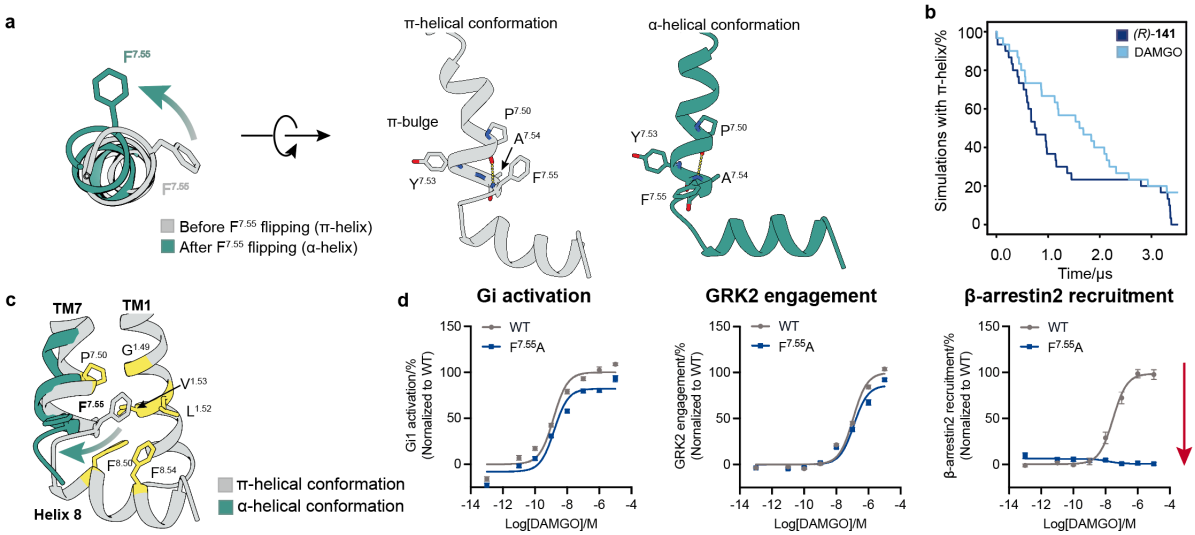

Fig. 4 | Conformation dynamics of TM7 in modulating β-arrestin recruitment. a, The rotation of $F^{7.55}$ influences the helical conformation of TM7, resulting in a release from π-helix into α-helix. **b,** Percentage of μOR MD simulations (n = 15) retaining a π-helix at the intracellular side of TM7 for receptors bound to *(R)*-**141** and DAMGO, respectively. **c,** π-bulge release is related to the rotation of $F^{7.55}$ out of a hydrophobic pocket (formed by residues in TM1, TM7, and Helix 8). **d,** Facilitating that π-bulge release by reducing the hydrophobicity at $F^{7.55}$ specifically abolishes DAMGO-induced β-arrestin recruitment, while having minimal impact on G protein activation and GRK2 engagement at the μOR.

Data are shown as mean ± S.E.M. of at least three independent replicates for panel **d**. The expression levels of each mutant are represented in Extend Data Fig.3J.

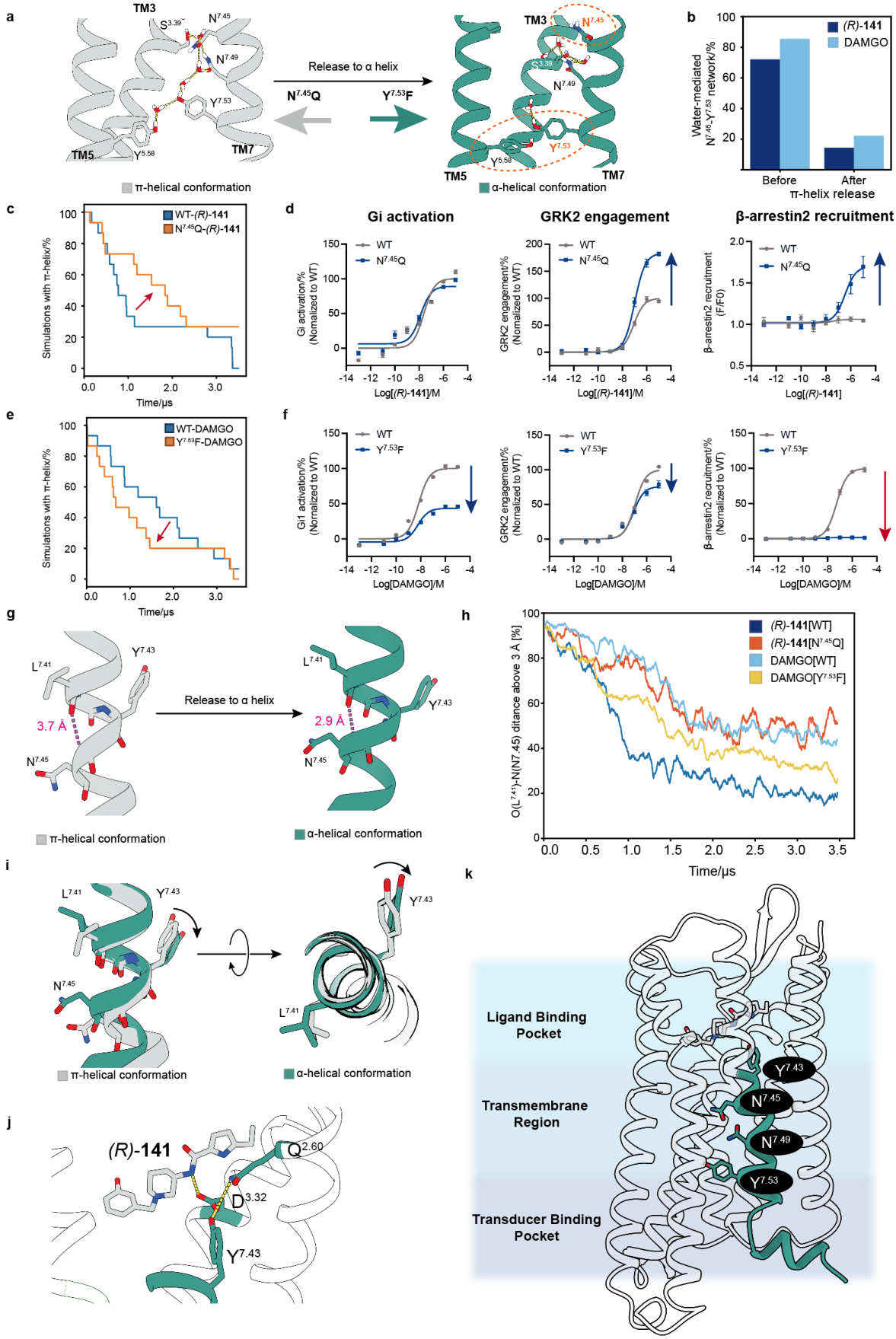

Fig.5 | *(R)*-141 modulates the dynamics of TM7 through a pYN motif. a, Water network connecting residues $N^{7.45}$ and $Y^{7.53}$ via TM7 rearranges after π-bulge release. **b,** Bar plot showing the percentage of frames exhibiting a water-mediated connection between $N^{7.45}$ and $Y^{7.53}$ before and after π-helix release, for simulations with *(R)*-**141** and DAMGO bound to the receptor, respectively. **c,** The $N^{7.45}Q$ substitution delays the π-bulge release in the presence of *(R)*-141. **d,** The $N^{7.45}Q$ mutation enhances the GRK2 engagement as well as the β-arrestin recruitment of *(R)*-**141**. **e,** The $Y^{7.53}F$ mutation accelerates the release of the π-bulge when bound to DAMGO. **f,** The $Y^{7.53}F$ mutation abolished DAMGO-induced β-arrestin recruitment while only less affecting G protein and GRK engagement. This suggests that the α-helical conformation of this segment hinders β-arrestin recruitment. **g,** Representative structural models illustrating the $L^{7.41}$-$N^{7.45}$ helical compaction during the π-to-α transition, highlighting the reduction in backbone hydrogen bond distance. **h,** Dwell time of the $L^{7.41}$-$N^{7.45}$ helical compaction across different simulation setups, quantified by the percentage of O ($L^{7.41}$)-N ($N^{7.45}$) distances exceeding 3 Å over time. These distinct structural profiles are tightly coupled to the pharmacological phenotypes of the wild-type and mutant μORs. **i,** Structural alignment demonstrating that the helical compaction is structurally coupled to the movement of the $Y^{7.43}$ side chain. (**J**) Detailed view of the orthosteric pocket revealing that *(R)*-**141** engages $Y^{7.43}$ through an extended polar interaction network involving $D^{3.32}$ and $Q^{2.60}$. **k,** The *(R)*-**141** triggers a spatial propagation cascade across the transmembrane region via the vertical "pYN motif" (comprising $Y^{7.43}$, $N^{7.45}$, $N^{7.49}$, and $Y^{7.53}$), effectively linking extracellular ligand recognition to intracellular transducer selection.

Data are shown as mean ± S.E.M. of at least three independent replicates for panels **d** and **f**. The expression levels of each mutant are represented in Extend Data Fig.3J.

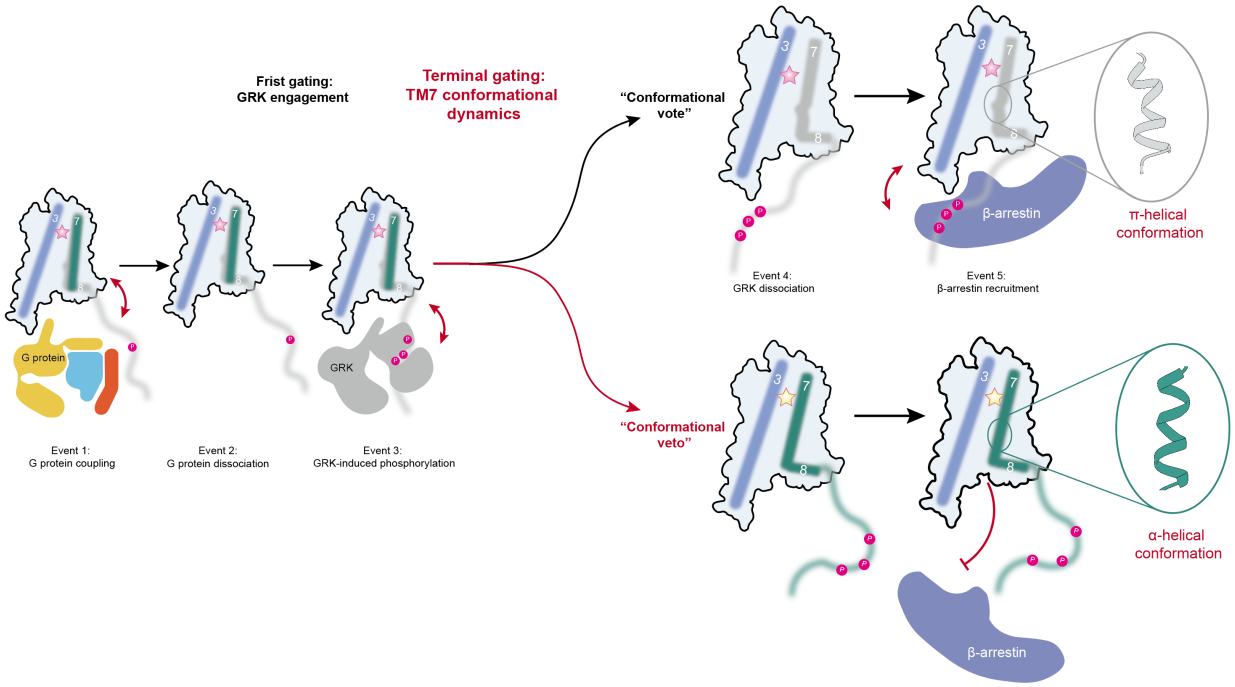

Fig.6 | Proposed sequential gating mechanism for μOR signaling transition. Due to the requirement of C-terminal phosphorylation, GRK engagement and subsequent receptor phosphorylation serve as the first gate in the transition from G protein signaling to β-arrestin recruitment. Following this, the conformational dynamics of TM7 function as a terminal gate, either facilitating recruitment through a "conformational vote" or preventing it via a "conformational veto."

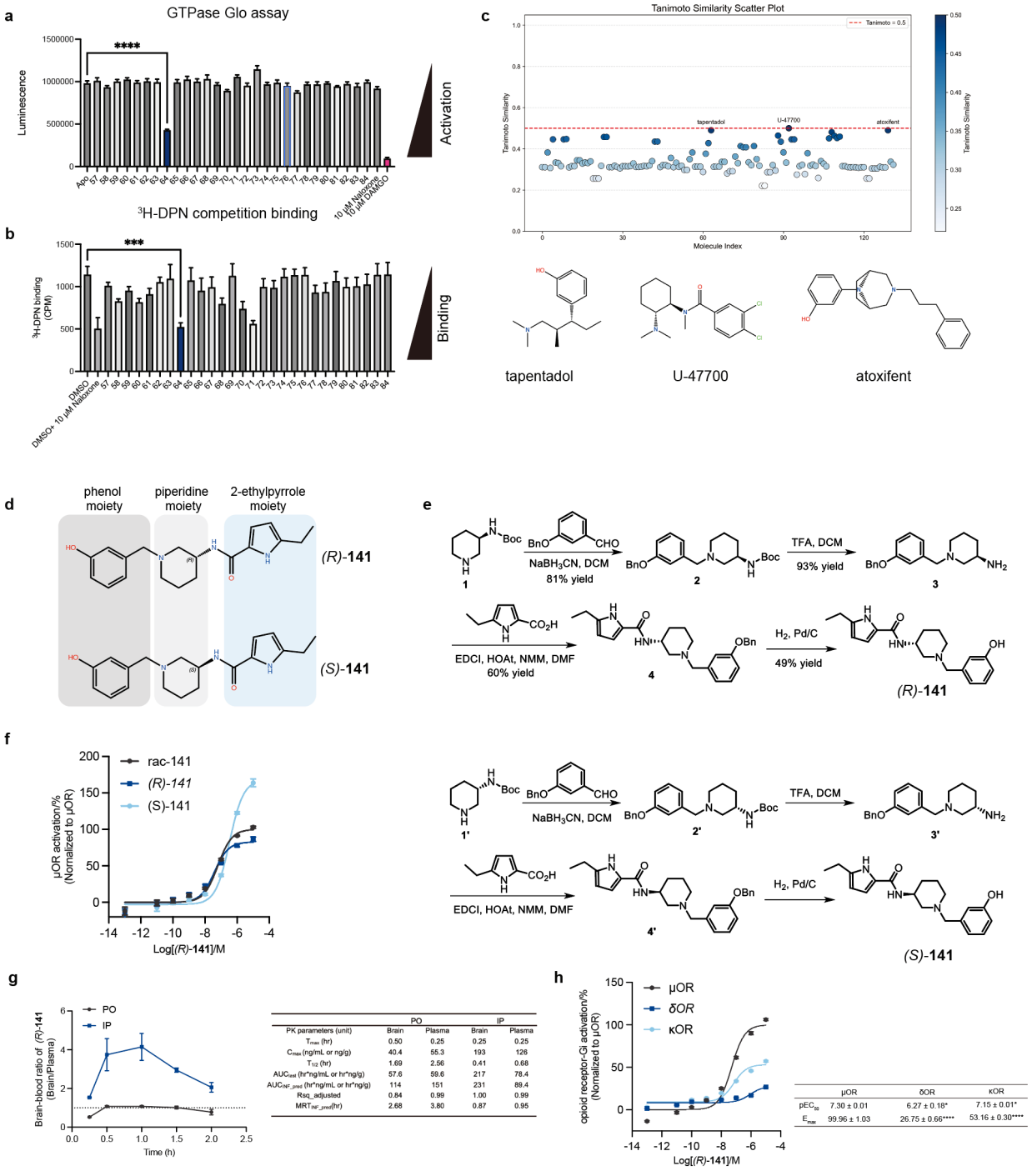

PK parameters (unit)	PO Brain	PO Plasma	IP Brain	IP Plasma
T_{max} (hr)	0.50	0.25	0.25	0.25
C_{max} (ng/mL or ng/g)	40.4	55.3	193	126
$T_{1/2}$ (hr)	1.69	2.56	0.41	0.68
AUC_{last} (hr*ng/mL or hr*ng/g)	57.6	59.6	217	78.4
AUC_{INF_pred} (hr*ng/mL or hr*ng/g)	114	151	231	89.4
Rsq_adjusted	0.84	0.99	1.00	0.99
MRT_{INF_pred}(hr)	2.68	3.80	0.87	0.95

	μOR	δOR	κOR
pEC_{50}	7.30 ± 0.01	6.27 ± 0.18*	7.15 ± 0.01*
E_{max}	99.96 ± 1.03	26.75 ± 0.66****	53.16 ± 0.30****

Extended Data Fig.1 | Discovery and pharmacological profile of *(R)*-141. a, Among the first 28 compounds identified from virtual screening, compound 64 exhibits agonistic activity toward μOR, as verified using a GTPase-Glo assay. Naloxone was used as a negative control, while DAMGO served as a positive control. **b,** Compound 64 binds to the orthosteric ligand-binding pocket of μOR. **c,** Compound 64 features a novel chemical scaffold compared to reported μOR agonists. Scaffold similarity is quantified by calculating the Tanimoto coefficient of compound 64

against other reported μOR agonists using the fingerprint. **d,** The single stereocenter at the piperidine moiety of *rac*-141. **e,** Syntheses of stereochemically pure *(R)*-**141** and (*S)*-**141**. **f,** (*R)*-**141** exhibit higher affinity and lower efficacy compared to (*R)*-**141**. **g,** Pharmacokinetic analysis indicates that *(R)*-**141** is enriched in the central nervous system following administration, suggesting strong blood-brain barrier penetration. **h,** *(R)*-**141** displays selectivity for μOR over δOR and κOR. Data are shown as mean ± S.E.M. of three independent replicates for **a,c,f,g-h.** Statistical significance was determined by unpaired t-test. ns $P > 0.05$, *$P < 0.05$, **$P < 0.01$.

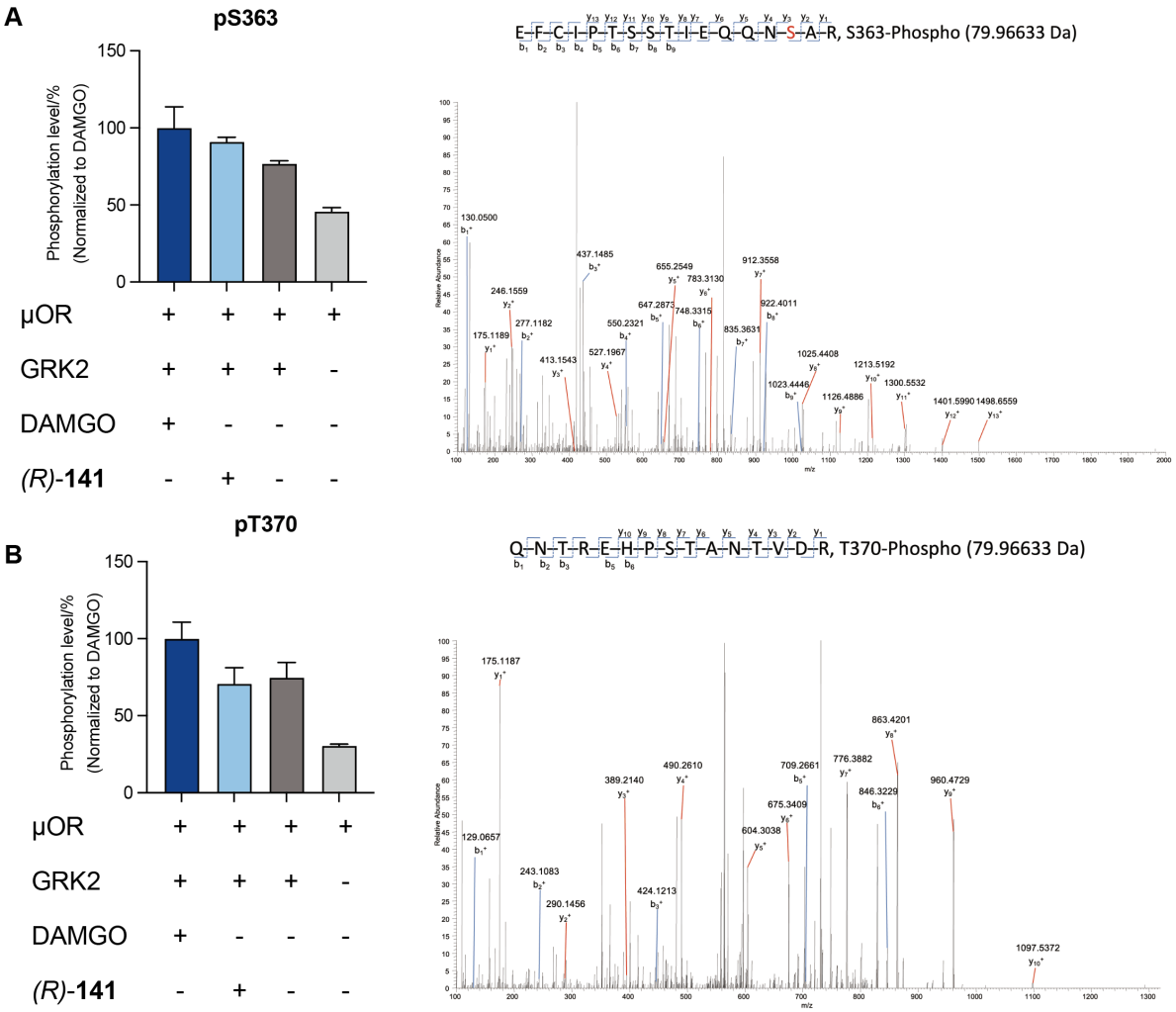

Extended Data Fig.2 | Phosphorylation of μOR upon activation by *(R)*-141. a-b, Phosphorylation levels of μOR at residues S363 (**a**) and T370 (**b**) induced by DAMGO or *(R)*-**141** in the presence of GRK2, as quantified by mass spectrometry. Representative spectra identifying the phosphorylated peptides are shown on the right. Data are shown as mean ± S.E.M. of three independent replicates.

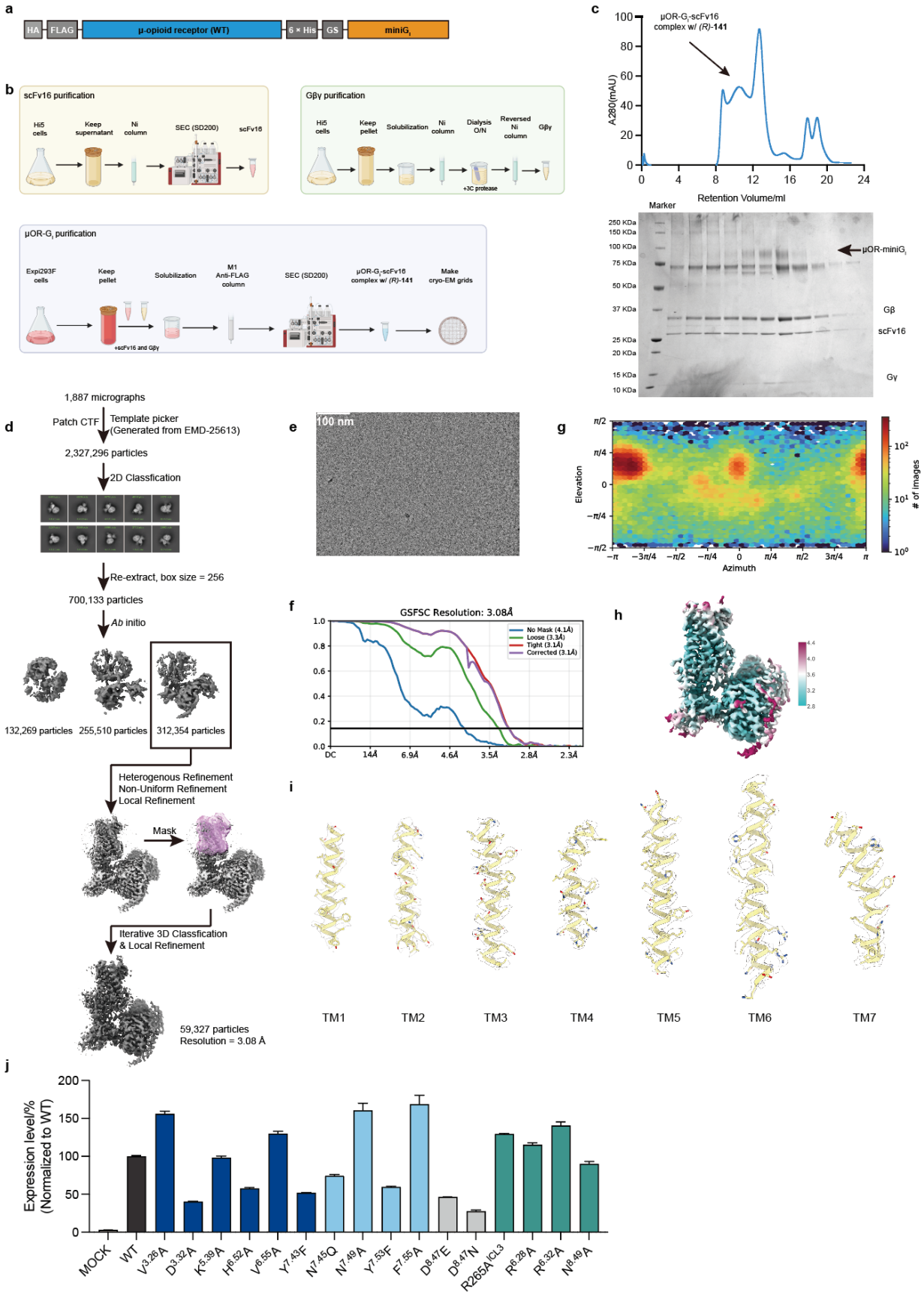

Extended Data Fig.3 | Structure determination of μOR-Gi-*(R)*-141 complex. a, The miniGi was fused to the C terminus of μOR for complex preparation. **b,** Schematic diagram of scFv16, Gβγ, and μOR-Gi complex purification, created with BioRender.com. **c,** Size-exclusion chromatography (SEC) purification and SDS-PAGE gel of the μOR-Gi-scFv16-*(R)*-**141** complex. **d**, Data processing workflow of μOR-Gi-scFv16-*(R)*-**141** complex, see methods for detail. **e,** Representative micrograph of the cryo-EM sample, scale bar = 100 nm. **f**, The Gold-standard Fourier Shell Correlation (GSFSC) curve indicates that the resolution of the final cryo-EM map of the μOR-Gi-scFv16-*(R)*-**141** complex is 3.08 Å. **g**, Angular distribution of the particles used for the final reconstruction. **h,** Local cryo-EM density of the μOR-Gi-scFv16-*(R)*-**141** complex. **i**, Cryo-EM density maps of the transmembrane helices of μOR. **j,** Expression level of each μOR mutant compared to the wild type receptor, quantified by cell surface staining. Data are shown as mean ± S.E.M. of three independent replicates.

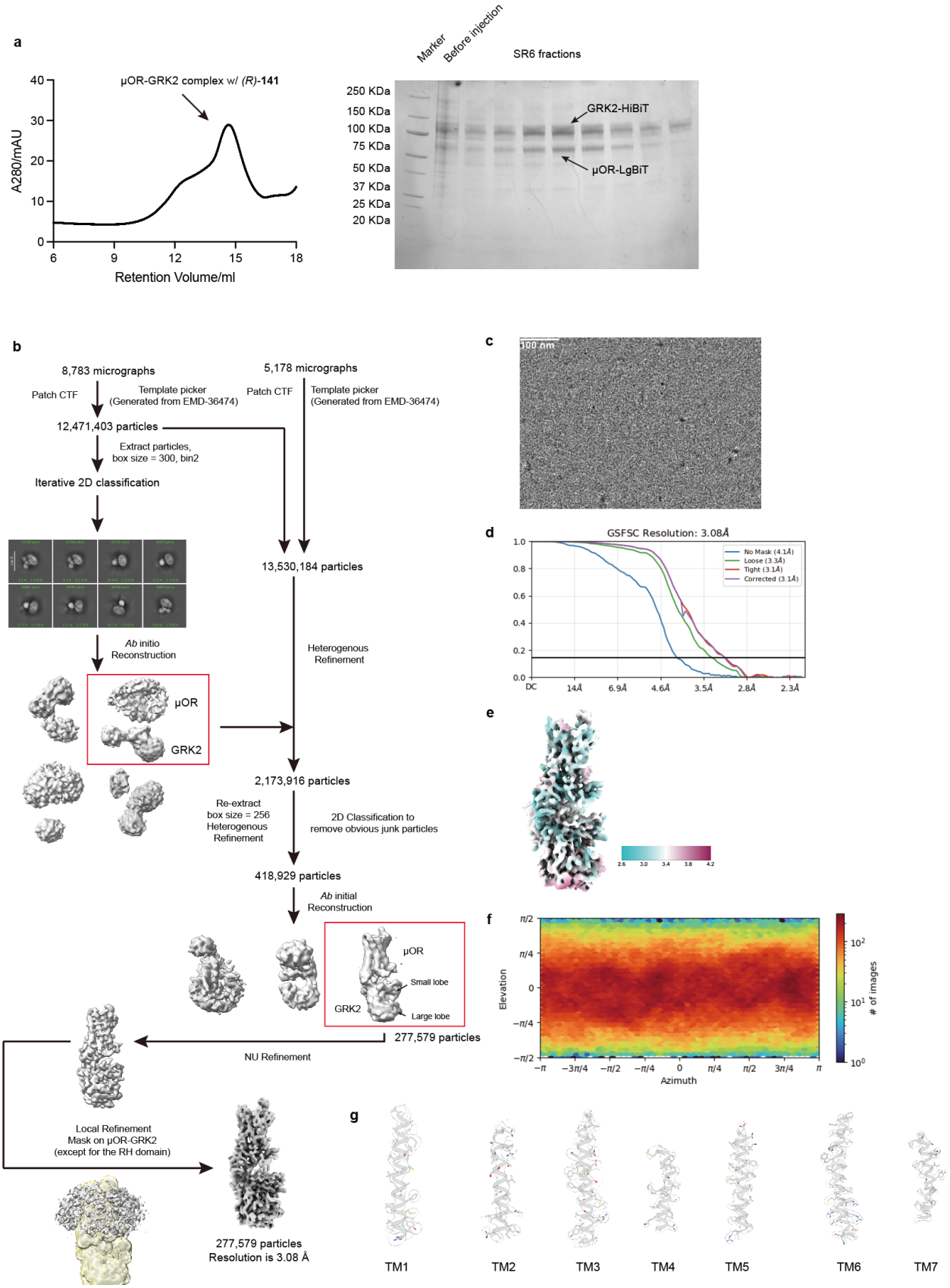

Extended Data Fig.4 | Structure determination of μOR-GRK2-*(R)*-141 complex. a, Size-exclusion chromatography (SEC) purification and SDS-PAGE gel of the μOR-GRK2-*(R)*-**141** complex. **b,** Data processing workflow of μOR-GRK2-*(R)*-**141** complex, see methods for detail. **c,** Representative micrograph of the cryo-EM sample, scale bar = 100 nm. **d,** The Gold-standard Fourier Shell Correlation (GSFSC) curve indicates that the resolution of the final cryo-EM map of the μOR-GRK2-*(R)*-**141** complex is 3.08 Å. **e,** Local cryo-EM density of the μOR-GRK2-*(R)*-**141** complex. **f,** Angular distribution of the particles used for the final reconstruction. **g,** Cryo-EM density maps of the transmembrane helices of μOR in the GRK2 complex.

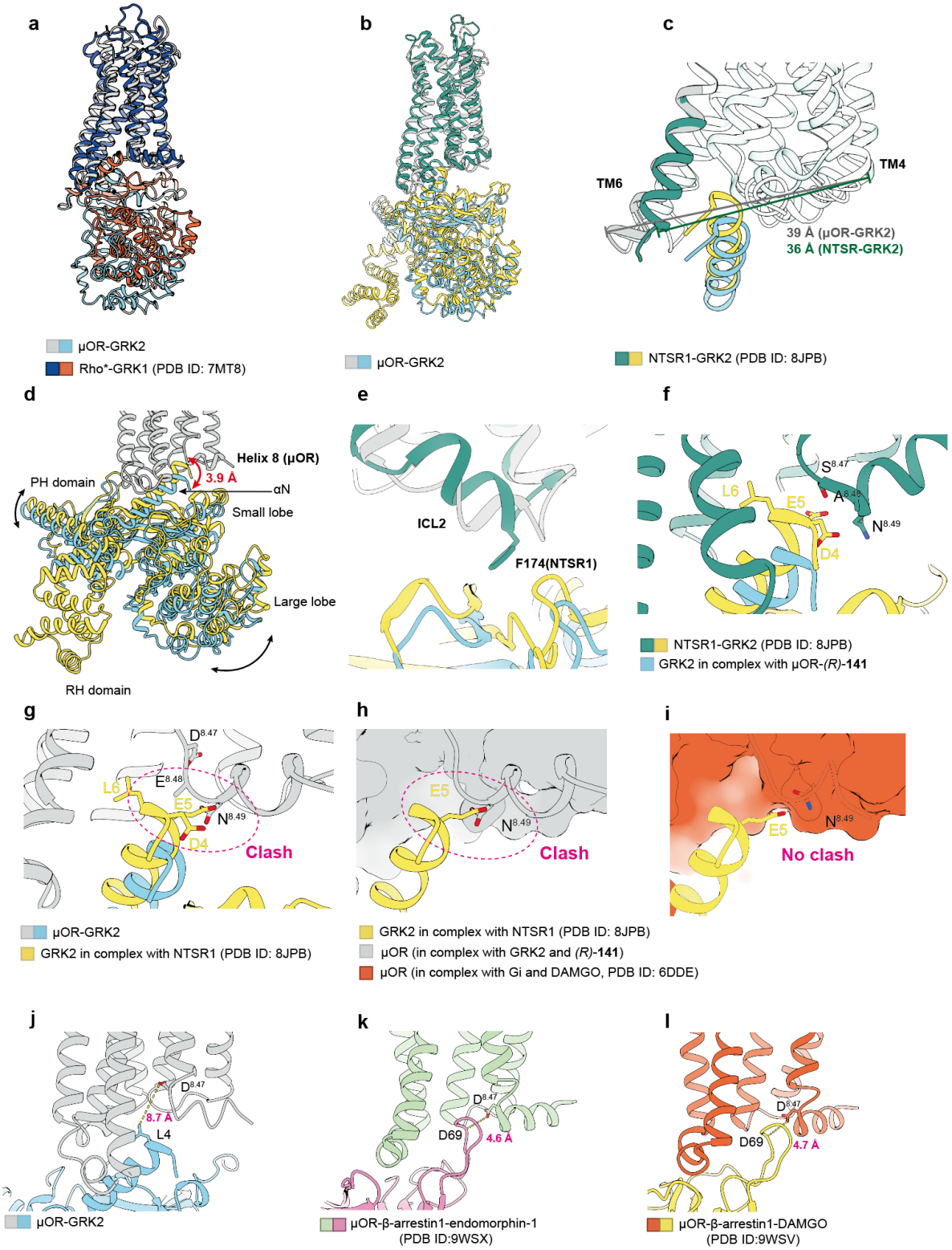

Extended Data Fig.5 | Structural analysis of μOR-GRK2-*(R)*-141 complexes. a, Structural alignment of μOR-GRK2-*(R)*-**141** with the Rho*-GRK1 complex (PDB ID: 7MT8). GRK1 and GRK2 adopt distinct conformations in these two structures. **b,** Structural alignment of μOR-

GRK2-*(R)*-**141** with the NTSR1-GRK2 complex (PDB ID: 8JPB). Both the receptor and GRK maintain a conserved conformation in these two structures. **c,** Compared to NTSR1, the TM6 of μOR exhibits a more pronounced outward movement in the μOR-GRK2-*(R)*-**141** complex. **d,** In the μOR-*(R)*-**141** complex, GRK occupies a shallower position. Additionally, the large lobe and PH domain of GRK2 undergo a significant interdomain twist. **e,** Differential ICL2 interactions: NTSR1 establishes direct contacts with GRK2 via its ICL2, an interface that is completely absent in the μOR. **f,** Structural alignment highlighting the distinct insertion depths of the GRK2 αN helix. The αN helix engages at a shallower depth in the μOR-*(R)*-**141** complex (blue) compared to the deeper insertion observed in the full agonist-bound NTSR1-GRK2 complex (yellow, PDB ID: 8JPB). **g-h,** Superposition of the NTSR1-bound GRK2 αN helix onto the μOR-*(R)*-**141** complex. Both cartoon (**g**) and surface (**h**) representations reveal that accommodating the GRK2 αN helix at the NTSR1-like depth would result in a severe steric clash (magenta dashed circle) with helix 8 (specifically $N^{8.49}$) of the μOR. (**i**) Superposition of the NTSR1-bound GRK2 αN helix onto the DAMGO-bound μOR structure (red, PDB ID: 6DDE). In contrast to the *(R)*-**141** state, the intracellular cavity of the DAMGO-bound state accommodates the deeper αN insertion without evident steric clashes. **j,** Detailed view of the μOR-GRK2 interface, showing a distance of 8.7 Å between $D^{8.47}$ of the receptor and L4 of GRK2. **k-l**, Detailed views of the μOR-β-arrestin1 interfaces in the endomorphin-1-bound state (**k**, PDB ID: 9WSX) and the DAMGO-bound state (**l**, PDB ID: 9WSV). The distances between $D^{8.47}$ and D69 (Cα) of β-arrestin1 are 4.6 Å and 4.7 Å, respectively. Collectively, these measurements verify that $D^{8.47}$ does not directly participate in transducer binding.

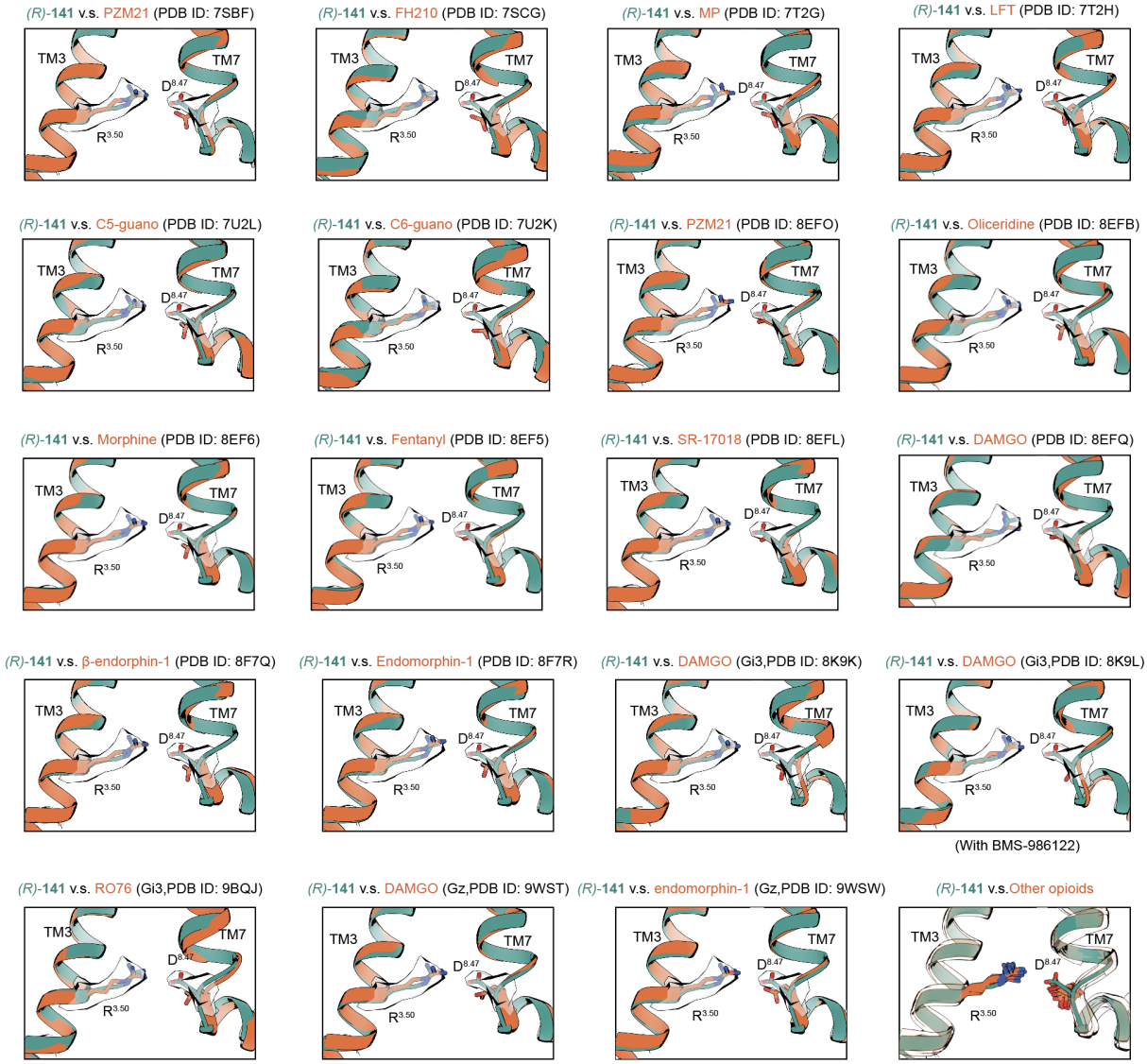

Extended Data Fig.6 | The $R^{3.50}$-$D^{8.47}$ ionic lock is absent in other resolved structure of μOR-G protein complex. Structure alignment of μOR-Gi-*(R)*-**141** (green) with other resolved structures of μOR-Gi/z complexes (orange) suggest the absence of this ionic lock. The cryo-EM density of $R^{3.50}$ and $D^{8.47}$ in the μOR-Gi-*(R)*-**141** complex shown in each panel supports the modeling of these two residues. Unless otherwise specified, all structures shown are μOR-Gi1 complexes.

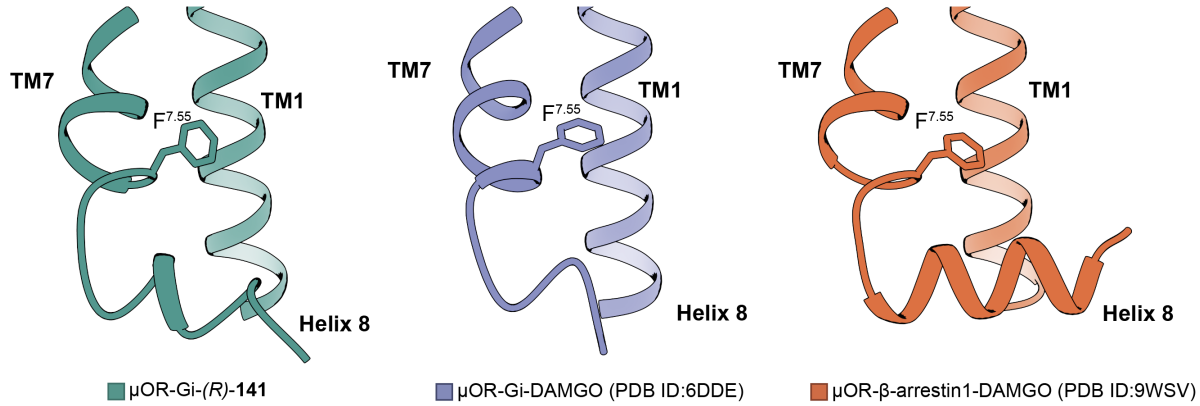

Extended Data Fig.7 | The orientation of $F^{7.55}$ in different structures. The $F^{7.55}$ positioned toward a pocket flanked by Helix 8 and TM1 in *(R)*-**141** and DAMGO-bound μOR structures.

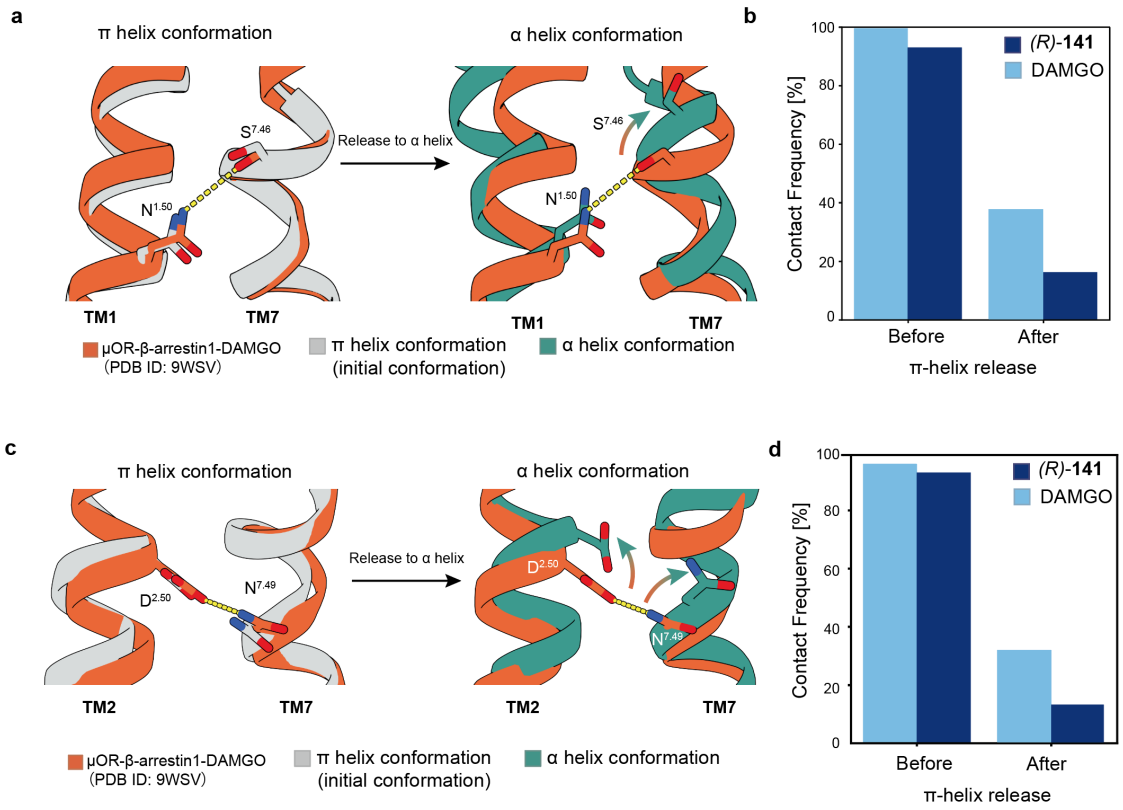

Extended Data Fig.8 | Temporal coupling between the loss of interactions and the π-bulge release of the TM7. a and c, Structural superpositions demonstrating that the transition from a π-helical to an α-helical conformation in TM7 directly breaks the $N^{1.50}$-$S^{7.46}$ (**a**) and $D^{2.50}$-$N^{7.49}$ (**c**) polar contacts. These interactions are fundamentally intact in the reference μOR-β-arrestin1 structure (PDB ID: 9WSV). **b and d,** MD simulation statistics confirm that the contact frequencies of $N^{1.50}$-$S^{7.46}$ (**b**) and $D^{2.50}$-$N^{7.49}$ (**d**) drop after the π-helix release across different ligand-bound states.

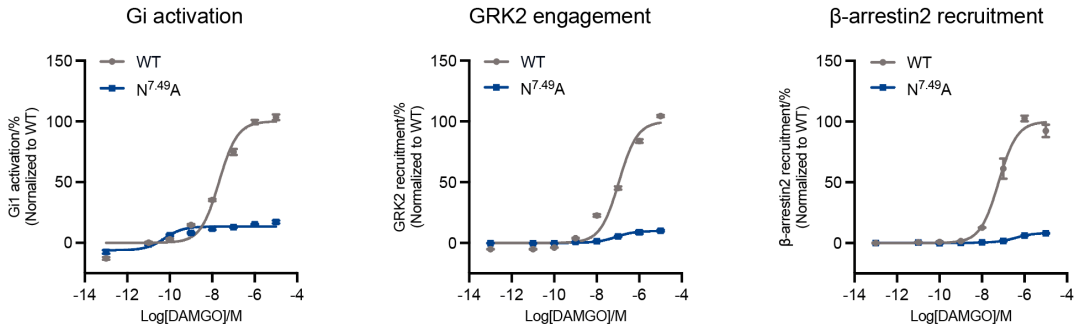

Extended Data Fig.9 | $N^{7.49}$ is crucial for the signal transduction of μOR. Substitution of $N^{7.49}$ into Alanine inhibits the signal transduction of μOR upon activation by DAMGO. Data are shown as mean ± S.E.M. of at least three independent replicates.

1454 **Extended Data Table 1. Cryo-EM data collection, refinement and validation statistics**

	μOR-Gi-*(R)*-**141** EMDB-69465 PDB 24EU	μOR-GRK2-*(R)*-**141** EMDB-69466 PDB 24EV
Data collection and processing		
Magnification	64,000	64,000
Voltage (kV)	300	300
Electron exposure (e–/Å^2)	50	50
Defocus range (μm)	-1.1-1.6	-1.1-1.6
Pixel size (Å)	1.08	1.08
Symmetry imposed	C1	C1
Initial particle images (no.)	2,327,296	13,530,184
Final particle images (no.)	59,327	277,579
Map resolution (Å)	3.08	3.08
FSC threshold	0.143	0.143
Map resolution range (Å)	2.77-49.99	2.57-27.49
Refinement		
Initial model used (PDB code)	6DDE	8EFQ and 9JPB
Model resolution (Å)		
FSC threshold	0.143	0.143
Model resolution range (Å)	3.0-3.3	2.8-4.1
Map sharpening *B* factor (Å^2)	-78.1	-112.6
Model composition		
Non-hydrogen atoms	8497	6316
Protein residues	1119	830
Ligands	1	2
B factors (Å^2)		
Protein	69.55	79.77
Ligand	73.50	73.36
R.m.s. deviations		
Bond lengths (Å)	0.004	0.003
Bond angles (°)	0.704	0.731
Validation		
MolProbity score	2.03	2.21
Clashscore	11.79	14.34
Poor rotamers (%)	1.38	0.96
Ramachandran plot		
Favored (%)	95.14	89.93
Allowed (%)	4.86	10.07
Disallowed (%)	0	0

1455

1456

1457